



UPPSALA
UNIVERSITET

*Digital Comprehensive Summaries of Uppsala Dissertations
from the Faculty of Medicine 1876*

Theranostics in Neuroendocrine Tumors

Somatostatin Receptor Imaging and Therapy

EZGI ILAN



ACTA
UNIVERSITATIS
UPSALIENSIS
UPPSALA
2022

ISSN 1651-6206
ISBN 978-91-513-1626-0
URN urn:nbn:se:uu:diva-486536

Dissertation presented at Uppsala University to be publicly examined in Rudbecksalen, Rudbecklaboratoriet, Dag Hammarskjölds väg 20, Uppsala, Friday, 2 December 2022 at 09:00 for the degree of Doctor of Philosophy (Faculty of Medicine). The examination will be conducted in English. Faculty examiner: Professor Peter Bernhardt (Department of Radiation Physics, Institute of Clinical Sciences, University of Gothenburg).

Abstract

Ilan, E. 2022. Theranostics in Neuroendocrine Tumors. Somatostatin Receptor Imaging and Therapy. *Digital Comprehensive Summaries of Uppsala Dissertations from the Faculty of Medicine* 1876. 61 pp. Uppsala: Acta Universitatis Upsaliensis. ISBN 978-91-513-1626-0.

Neuroendocrine tumors (NETs) are characterized by cellular overexpression of somatostatin receptors (SSTR), which allows for the use of radiolabeled somatostatin analogs (SSA) for both imaging and therapy. Because NETs often are diagnosed at a metastatic stage, curative surgery is not possible. Monthly long-acting SSA preparation constitutes first-line therapy for low-grade small-intestinal NETs and pancreatic NETs. Peptide receptor radionuclide therapy (PRRT), with radiolabeled SSAs such as ^{177}Lu -DOTATATE, has been shown to be an effective therapeutic alternative for NETs, improving symptoms and quality of life. The gold-standard method for SSTR imaging and diagnosis of NETs is positron emission tomography (PET) using Gallium-68 (^{68}Ga)-labeled SSAs, such as ^{68}Ga -DOTATOC and ^{68}Ga -DOTATATE. The tumor standardized uptake value (SUV) has been proposed both as a marker of SSTR tumor density and a tool for evaluating therapy response. Changes of tumor SUV on ^{68}Ga -DOTATOC- and DOTATATE-PET have, however, not been shown to correlate with the patient outcome.

This thesis is based on five original papers, evaluating the relation between tumor-absorbed dose and tumor shrinkage and developing novel theranostic methods in which quantitative PET imaging with ^{68}Ga -DOTATATE and ^{68}Ga -DOTATOC is used to optimize PRRT with ^{177}Lu -DOTATATE in NET patients.

A high and significant positive correlation was found between tumor-absorbed dose and tumor shrinkage in pancreatic NETs treated with ^{177}Lu -DOTATATE. Furthermore, it was found that tumor SUV in ^{68}Ga -DOTATATE and ^{68}Ga -DOTATOC failed to correlate linearly with the net influx rate (K_i), assumed to reflect the SSTR density, due to low tracer availability in blood for high K_i values. SUV blood was significantly higher in tumors with high K_i (>0.2) than in tumors with low K_i , and it was found that the tumor-to-blood ratio (TBR) correlates linearly with K_i . Thus, both K_i and TBR may be used as tools to monitor NET therapy response rather than SUV. It was also found that parametric K_i images, illustrating K_i at the voxel level, provide higher tumor-to-liver contrast than static whole-body PET images. Further, it was found that administration of a single dose of cold peptide pre-PRRT with ^{177}Lu -DOTATATE gave rise to faster recycling of SSTRs in tumors than in normal organs. A linear relation was found for tumor SUV and early K_i , between ^{68}Ga -DOTATATE-PET and ^{177}Lu -DOTATE-SPECT; however, the kinetics for ^{68}Ga -DOTATATE could not be used for predicting that of ^{177}Lu -DOTATATE because of tumor clearance of ^{177}Lu -DOTATATE at late time interval.

In conclusion, quantitative PET imaging with ^{68}Ga -DOTATATE and ^{68}Ga -DOTATOC shows great potential for both evaluating therapy response and optimizing PRRT with ^{177}Lu -DOTATATE.

Keywords: ^{177}Lu -DOTATATE, ^{68}Ga -DOTATATE, ^{68}Ga -DOTATOC, PRRT, Theranostics, PET/CT, SPECT/CT, Neuroendocrine tumors, Somatostatin receptors

Ezgi Ilan, Department of Surgical Sciences, Radiology, Akademiska sjukhuset, Uppsala University, SE-75185 Uppsala, Sweden.

© Ezgi Ilan 2022

ISSN 1651-6206

ISBN 978-91-513-1626-0

URN urn:nbn:se:uu:diva-486536 (<http://urn.kb.se/resolve?urn=urn:nbn:se:uu:diva-486536>)

To my family

List of Papers

This thesis is based on the following papers, which are referred to in the text by their Roman numerals.

- I. Ilan, E., Sandström, M., Wassberg, C., Sundin, A., Eriksson, B., Granberg, D. and Lubberink, M. (2015) Dose response of pancreatic neuroendocrine tumors treated with peptide receptor radionuclide therapy using ^{177}Lu -DOTATATE. *Journal of Nuclear Medicine*, 56(2):177-182
- II. Ilan, E., Sandström, M., Velikyan, I., Sundin, A., Eriksson, B. and Lubberink, M. (2017) Parametric net influx rate images of ^{68}Ga -DOTATOC and ^{68}Ga -DOTATATE: Quantitative Accuracy and improved image contrast. *Journal of Nuclear Medicine*, 58(5):744-749
- III. Ilan, E., Velikyan, I., Sandström, M., Sundin, A. and Lubberink, M. (2020) Tumor-to-blood ratio for assessment of somatostatin receptor density in neuroendocrine tumors using ^{68}Ga -DOTATOC and ^{68}Ga -DOTATATE. *Journal of Nuclear Medicine*, 61(2):217-221
- IV. Jahn, U.*, Ilan, E.*, Velikyan, I., Fröss-Baron, K., Lubberink, M. and Sundin, A. (2021) Receptor depletion and recovery in small-intestinal neuroendocrine tumors and normal tissue after administration of a single intravenous dose of octreotide measured by ^{68}Ga -DOTATOC PET/CT. *EJNMMI Research*, 11(1):118
- V. Ilan, E., Velikyan, I., Sandström, M., Andersson, C., Jahn, U., Sundin, A. and Lubberink, M. (2022) Comparison of ^{68}Ga -DOTATATE and ^{177}Lu -DOTATATE kinetics in neuroendocrine tumors. *Submitted*

Reprints were made with permission from the respective publishers.

List of Additional Papers

The following papers are not included in the thesis.

- i. Sandström, M., Ilan, E., Karlberg, A., Johansson, S., Freedman, N. and Garske-Román, U. (2015) Method dependence, observer variability and kidney volumes in radiation dosimetry of ^{177}Lu -DOTA-TATE therapy in patients with neuroendocrine tumors. *EJNMMI Physics*, 2(1):24
- ii. Hsu, D. F. C., Ilan, E., Peterson, W. T., Uribe, J., Lubberink, M. and Levin, C. S. (2017) Studies of a Next-Generation Silicon-Photomultiplier-Based Time-of-Flight PET/CT System. *Journal of Nuclear Medicine*, 58(9):1511-1518
- iii. Lindström, E., Sundin, A., Trampal, C., Lindsjö, L., Ilan, E., Danfors, T., Antoni, G., Sörensen, J. and Lubberink, M. (2018) Evaluation of Penalized-Likelihood Estimation Reconstruction on a Digital Time-of-Flight PET/CT Scanner for ^{18}F -FDG Whole-Body Examinations. *Journal of Nuclear Medicine*, 59(7):1152-1158
- iv. Jahn, U., Ilan, E., Sandström, M., Garske-Román, U., Lubberink, M. and Sundin, A. (2020) ^{177}Lu -DOTATATE Peptide Receptor Radionuclide Therapy: Dose Response in Small Intestinal Neuroendocrine Tumors. *Neuroendocrinology*, 110(7-8):662-670
- v. Lubberink, M., Wilking, H., Öst, A., Ilan, E., Sandström, M., Andersson, C., Fröss-Baron, K., Velikyan, I. and Sundin, A., (2020) In Vivo Instability of ^{177}Lu -DOTATATE During Peptide Receptor Radionuclide Therapy. *Journal of Nuclear Medicine*, 61(9):1331-1340
- vi. Jahn, U., Ilan, E., Sandström, M. Lubberink, M., Garske-Román, U. and Sundin, A. (2021) Peptide Receptor Radionuclide Therapy (PRRT) with ^{177}Lu -DOTATATE; Differences in Tumor Dosimetry, Vascularity and Lesion Metrics in Pancreatic and Small Intestinal Neuroendocrine. *Cancers*, 13(5):962

Contents

| | |
|---|----|
| Introduction..... | 11 |
| Neuroendocrine tumors | 11 |
| Somatostatin receptors | 12 |
| Imaging of NETs..... | 13 |
| Diagnosis of NETs..... | 13 |
| Characteristics of ⁶⁸ Ga | 13 |
| Principles of radionuclide imaging..... | 14 |
| Gamma camera imaging..... | 14 |
| PET imaging..... | 15 |
| Partial volume effect..... | 21 |
| Treatment of NETs..... | 21 |
| Peptide receptor radionuclide therapy | 22 |
| Characteristics of ¹⁷⁷ Lu | 22 |
| Treatment and imaging with ¹⁷⁷ Lu-DOTATATE | 23 |
| Dosimetry | 23 |
| Pre-therapy dosimetry..... | 25 |
| Treatment follow up of NETs | 26 |
| Aims of the thesis..... | 27 |
| Material and methods..... | 28 |
| Study population | 28 |
| Data acquisition..... | 28 |
| Paper I..... | 28 |
| Paper II & III | 29 |
| Paper IV..... | 29 |
| Paper V | 30 |
| Data analysis | 31 |
| Volume definition..... | 31 |
| Dosimetry and best response (I) | 31 |
| Kinetic analysis (II-V) | 32 |
| Statistical analysis..... | 33 |
| Results..... | 34 |
| Paper I | 34 |
| Paper II..... | 35 |
| Paper III..... | 38 |

| | |
|--|----|
| Paper IV | 39 |
| Paper V..... | 42 |
| Discussion..... | 45 |
| Concluding remarks | 49 |
| Future perspectives | 50 |
| Populärvetenskaplig sammanfattning | 51 |
| Acknowledgement | 54 |
| References..... | 56 |

Abbreviations

| | |
|--------|---|
| 1TCM | Single tissue compartment model |
| 2TCM | Two tissue compartment model |
| ACDF | Activity concentration dose factor |
| BFM | Basis function method |
| CT | Computed tomography |
| DF | Dose factor |
| FOV | Field of view |
| IDID | Image derived input function |
| K_i | Net influx rate |
| NEC | Neuroendocrine carcinoma |
| NEN | Neuroendocrine neoplasm |
| NET | Neuroendocrine tumor |
| NLR | Nonlinear regression |
| p.i. | post injection |
| PET | Positron emission tomography |
| PNET | Pancreatic neuroendocrine tumor |
| PRRT | Peptide receptor radionuclide therapy |
| PVE | Partial volume effect |
| ROI | Region of interest |
| S | Pre-calculated dose conversion factor from MIRD |
| SSA | Somatostatin analog |
| SI-NET | Small-intestinal neuroendocrine tumor |
| SIME | Simultaneously estimation fit |
| SPECT | Single photon emission computed tomography |
| SSTR | Somatostatin receptors |
| SUV | Standardized uptake value |
| TBR | Tumor-to-blood ratio |
| TAC | Time activity curve |
| TIA | Time integrated activity |
| VOI | Volume of interest |

Introduction

Malignant tumors share several specific sets of hallmarks (1). However, despite shared characteristics and common features, it is known that cancer is a heterogeneous disease where tumor response to therapy can vary both intra- and interpatient. Lower success rates are therefore obtained in standardized cancer therapies where it is assumed that “one-size-fits-all.” The ultimate goal of cancer treatment is to cure the patient. However, for solid tumors, this is only possible at an early stage, mainly through surgery, and with options for adjuvant and neoadjuvant chemotherapy and external beam radiation therapy. Because many patients are diagnosed at an advanced stage, a cure is generally not possible, and the treatment options, such as surgery, external beam therapy, and chemotherapy, are merely palliative (2,3). This thesis focuses on theranostics in patients with neuroendocrine tumors (NETs) overexpressing somatostatin receptors using somatostatin receptor imaging with ⁶⁸Ga-DOTA-TATE and/or ⁶⁸Ga-DOTATOC and subsequent therapy with ¹⁷⁷Lu-DOTA-TATE.

Neuroendocrine tumors

Neuroendocrine neoplasms (NENs) are a heterogeneous group of tumors that arise from the diffuse endocrine system of cells distributed throughout the body (4). NENs include both well-differentiated neuroendocrine tumors (NETs) with low mitotic activity and poorly differentiated neuroendocrine carcinomas (NECs) with high mitotic activity. The heterogeneity of NENs depends both on traits from the organ site of the primary tumor and its neuroendocrine characteristics, such as SSTR expression and hormonal production. NETs are characterized based on primary tumor origin, such as pancreatic NETs (PNETs), small-intestinal NETs (SI-NETS), and rectal NETs. These are further divided based on their tumor grade, the proportion of proliferating tumor cells in the tumor determined by the proliferation marker Ki-67 and functionality. Well-differentiated tumors with Ki-67 index $\leq 2\%$ are classified as a grade 1 (G1), 3-20 % as grade 2 (G2), and $> 20\%$ as grade 3 (G3), whereas low differentiated G3 tumors are denoted neuroendocrine cancers (NEC). Functioning tumors produce hormones, which give rise to a hormonal syndrome, whereas nonfunctioning tumors do not. The clinical symptoms arising

from the presence of hormone secretion depend on the main hormone that is secreted (4,5). The clinical appearance of the disease depends on the primary tumor site, its local growth, and its hormonal status (i.e., whether the tumor is functioning and secrete peptides or is nonfunctioning). Most NETs are non-functioning and appear clinically when they are large and/or have metastasized to the liver (6), and approximately 60–80 % of NETs are metastatic at the time of diagnosis (7). Diagnostic delay is common (5–7 years) and precludes curative therapy in many patients since this can only be performed at an early stage (6,8).

Pancreatic NETs (PNETs) are mainly slow-growing and non-functioning, although hormonal production may be detected biochemically (9). Functional PNETs will, however, result in characteristic symptoms based on their specific hormonal overproduction. Insulinoma, the most common functional PNET, will result in hypoglycemia, glucagonoma will result in hyperinsulinemia, and VIPoma (tumor excreting vasoactive intestinal peptide) in watery diarrhea, hypokalemia, and achlorhydria (WDHA syndrome). Because the majority of PNETs are non-functioning and slow-growing, patients tend to seek medical attention at a later stage because of local pressure or tumor overgrowth on adjacent organs. Thus, late detection leads to a higher tumor stage with metastasis present at diagnosis (10,11).

SI-NETs are slow-growing tumors that often metastasize to the liver and regional lymph nodes. Approximately 40–60% of SI-NETs produce serotonin, which may give rise to flushing, diarrhea, and abdominal pain, together with right-sided heart failure (12). Many SI-NET patients experience uncharacteristic and variable symptoms that are easily misinterpreted as those from common benign diseases and, therefore, on average, cause a 5–7-year delay in diagnosis. Consequently, metastatic spread is common at the time of diagnosis (7,13).

Even though NETs have been considered to be rare, analysis from the North American Surveillance, Epidemiology, and End Results registry data shows that the NET incidence increased 5-fold over the past three decades from 1.09/100,000 in 1973 to 5.25/100,000 in 2004 as a result of the introduction of new diagnostic techniques and increased awareness (6,14). Because many patients live for many years, the prevalence is considerably higher, approximately 30/100,000. The overall survival (5 years) is about 75% and depends primarily on the stage and grade of the tumor (14).

Somatostatin receptors

Most NETs are characterized by cellular overexpression of somatostatin receptors (SSTRs) (15). These receptors are G-protein-coupled transmembrane receptors (16) expressed in many tissues throughout the body (such as kidneys, pancreas, spleen, and liver) (17). In humans, five subtypes of SSTR have

been identified (SSTR 1–SSTR 5), and the most frequently overexpressed in NETs is SSTR 2 (18).

The SSTRs in NETs are attractive targets both for imaging and therapy applications, given that the SSTR density in tumors is higher than that in most normal tissues. The first synthesized somatostatin analog (SSA) is the peptide octreotide, which has a high affinity for SSTR 2 and moderate affinity for SSTR 3 and 5. Lanreotide is another SSA with similar SSTR subtype affinities as octreotide (19).

Imaging of NETs

Diagnosis of NETs

NET overexpression of SSTRs has allowed for the development of radio-labeled SSAs for NET diagnosis. By labeling SSAs with radioisotopes, SSTR-expressing NETs can be targeted and visualized by imaging with either a gamma camera or positron emission tomography (PET).

Historically, SSTR scintigraphy with a radiolabeled isotope was first performed in 1989 with ^{123}I -octreotide and reported by Krenning et al. (20). Due to its drawbacks, ^{123}I was replaced with ^{111}In (21) and to achieve a stable conjugation between the SSA and the radioisotope, ^{111}In , was labeled with octreotide via the chelating agent (chelator) diethylene triamine pentaacetic acid (DTPA). For many years, ^{111}In -DTPA-octreotide (Octreoscan®) imaging with a gamma camera (both two- and three-dimensions) comprised the gold standard for NET diagnosis (21). However, current guidelines no longer recommend SSTR imaging with a gamma camera (22)

During the past decade, PET in combination with computed tomography, PET/CT, with ^{68}Ga -labeled SSAs such as ^{68}Ga -DOTATOC, ^{68}Ga -DOTANOC, and ^{68}Ga -DOTATATE, has gradually replaced SSTR scintigraphy with ^{111}In -DTPA-octreotide, and become the standard method for SSTR imaging of NETs (22-27). This is due to better sensitivity and image quality combined with considerably shorter acquisition time (24,28) with PET/CT as compared to SPECT/CT. PET/CT shows specificity and sensitivity well above 90 %, exceeding that of octreoscan and CT (22-27). No clinically relevant difference in sensitivity was found between different SSAs (DOTATOC, DOTANOC, and DOTATATE) (29-31). Barrio et al. (32) showed that PET/CT findings with ^{68}Ga -DOTATOC, ^{68}Ga -DOTANOC, and ^{68}Ga -DOTATATE resulted in management changes in 44% of the patients.

Characteristics of ^{68}Ga

^{68}Ga disintegrates by positron emission (β^+) to a ground state of ^{68}Zn (87.7%) with a half-life of 68 minutes. The maximum and mean β^+ energies of the

positron emission are 633.5 and 249.3 keV, respectively. ^{68}Ga also decays with a positron branch to an excited state of ^{68}Zn (1.2 %) which is followed by a prompt gamma emission of 1077 MeV to the ground state of ^{68}Zn (33).

Principles of radionuclide imaging

The concept of radionuclide imaging is to obtain an image of the radiolabeled pharmaceutical (radiopharmaceutical) distributed within the patient body. This is performed by recording the gamma-ray emission from the radioisotope with external radiation detectors placed outside the patient at different locations. For photon-emitting radioisotopes, a gamma camera is used to detect the radioactive distribution and for positron-emitting radioisotopes, a PET scanner is used.

Gamma camera imaging

The gamma camera is a non-invasive, molecular imaging technique visualizing the distribution of a photon-emitting radioactive isotope. The gamma camera detects the incoming gamma rays from the patient with a specific energy, perpendicular to the detector. The camera generally consists of two detector heads, and the basic principle of a gamma camera is shown in Figure 1. The detector consists of a large scintillation crystal with a high cross section for photoelectric interactions, that absorbs the photons and converts the absorbed photon energy into visible light. A collimator is placed in front of the crystal to define the direction of detected gamma rays. When a photon is absorbed by the detector, due to the collimator, it is known that the decay took place along a line in the direction of the collimator holes (more-or-less perpendicular to the detector). However, it is not known at what distance, along this line, the disintegration took place. The collimator only let through photons that travels in a certain direction, and without the collimator, the direction of the incident photons is unknown, and the gamma camera cannot provide an image of the radioactive distribution of the radiopharmaceutical. By controlling which gamma rays are accepted, the collimator forms a projected image of the radiopharmaceutical distribution on the crystal.

A gamma camera can acquire both two- and three-dimensional images of the radioactivity distribution within the patient. Planar images (static or whole-body) are two-dimensional images of a three-dimensional radioactivity distribution. If patient images are acquired by rotation of the detector heads around the patient at different angles, three-dimensional images of the radioactivity distribution can be acquired. This is called single photon emission computed tomography (SPECT) (34).

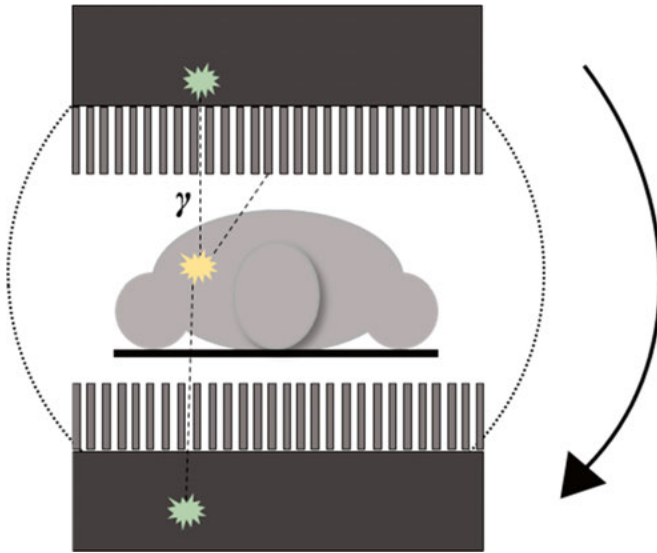


Figure 1. Gamma-ray photons (γ) are emitted from a radioactive isotope distributed within the patient and detected by the collimated scintillation crystal (detector), which can rotate around the patient (SPECT imaging). Only photons that are more-or-less perpendicular to the detector plane can pass through the collimators which determines the line of photon emission. The crystal absorbs the photons and converts the absorbed photon energy into visible light.

PET imaging

PET is a non-invasive, molecular imaging method that provides visualization and quantification of biological and physiological processes (metabolic process, blood flow, receptor binding, etc.) within the body. Through administration of molecules in tracer amount labeled with positron-emitting radionuclide, such as ^{11}C , ^{15}O , ^{18}F , and ^{68}Ga , the distribution of these molecules in a tissue of interest can be imaged in the PET scanner, without affecting the biological system of interest (34). The most commonly used tracer is ^{18}F -fluoro-2-deoxy-D-glucose (^{18}F -FDG), which measures glucose metabolism in tissue (35).

Positron decay occurs when the nucleus has an excess of protons. The proton decays into a neutron and positron (a neutrino is also emitted, balancing the energy and momentum). The emitted positron first travels a short distance (of the order of millimeters) from the initial decay site while losing its kinetic energy. The positron then recombines with an electron, a positron-electron annihilation occurs, and their rest masses are converted into a pair of annihilation photons. The energy of the emitted photons is 511 keV, and they are emitted simultaneously in nearly opposite directions ($180 \pm 0.3^\circ$) depending on the energy and range of the positron. The principle of PET is based on the coincidence detection of two annihilation photons (produced from positron

decay) that are emitted in opposite directions. The PET scanner counts this coincidence event between pairs of detectors (almost simultaneously), and the straight line connecting the two detectors is called line of response. This line of response gives an indication of where the positron-electron annihilation occurred. The PET scanner consists of rings of detector blocks, with each detector element working in coincidence to record annihilation events. A simplified illustration of the basic principle of PET imaging is shown in Figure 2.

The recorded coincidence events on a PET scanner are reconstructed into a tomographic (three-dimensional) image illustrating the tissue distribution of the tracer, in units of radioactivity concentration in tissue (Bq/mL), after correction for several factors, such as random and scatter coincidence, attenuation, decay and dead time (34).

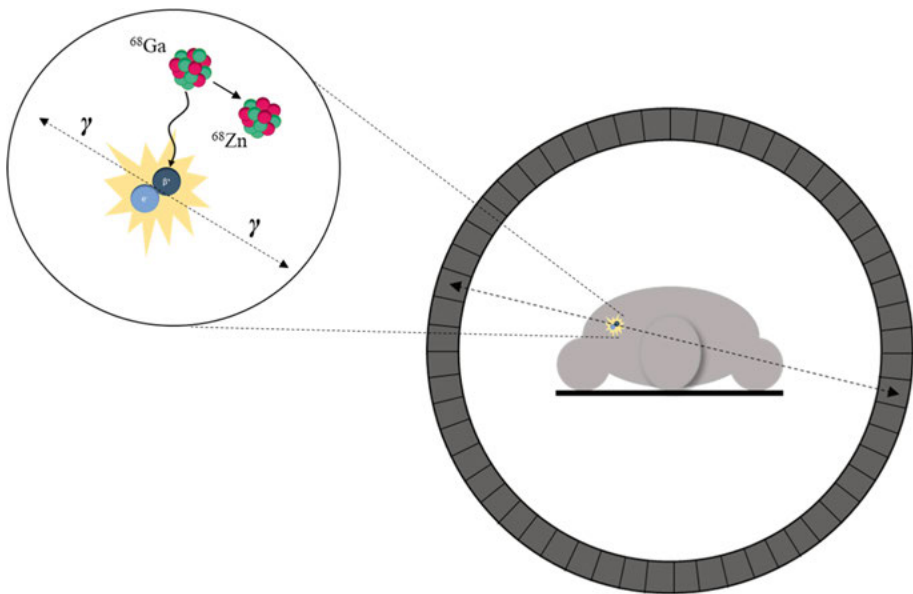


Figure 2. Schematic illustration of positron emission, positron-electron annihilation, and the subsequent coincidence detection in the PET scanner. The unstable nuclei decay emitting a positron which traverses a distance while losing its kinetic energy before it annihilates with an electron and creates two photons with an energy of 511 keV that are detected by the ring of detectors around the patient. The photons are emitted 180° apart ($\pm 0.3^\circ$).

Quantification

PET images can both be acquired as static images acquired at a specific time post-injection (p.i.), illustrating the average radioactivity concentration distribution within the patient or as dynamic images, where the data is collected in a series of time windows, so-called time frames, directly upon injection.

Static PET images are interpreted both visually and quantitatively. To read static PET images, standardized uptake value (SUV), a unitless

semiquantitative parameter, measuring the tracer uptake in the PET image relative to the injected activity and distribution within the patient, was introduced. SUV is defined as follows:

$$SUV = \frac{C_{PET}}{A/W} \quad (1)$$

where C_{PET} is the activity concentration in a region or volume of interest (ROI or VOI), A is the injected activity, and W is either patient body weight (mostly used), body surface area or lean body mass. SUV is a parameter representing the distribution of the injected tracer (relative to uniform distribution); thus, SUV of 1 implicates an even distribution of the injected tracer in the entire body. The SUV parameter is mostly used for oncology examinations with ^{18}F -FDG, to facilitate tissue characterization and to monitor the effect of oncological therapies (36-38).

In dynamic images, the rate of change of tracer distribution (i.e., change of radioactivity concentration) over time throughout the course of the PET study can be followed. The tracer concentration can be followed and measured as a function of time (38). From the dynamic scan, time-activity curves (TACs) can be obtained, illustrating the change of activity concentration over time in a specific VOI or voxel, as illustrated in Figure 3. The TAC can illustrate uptake, binding to a specific target such as a tumor receptor, retention, and clearance of the tracer over time (39).

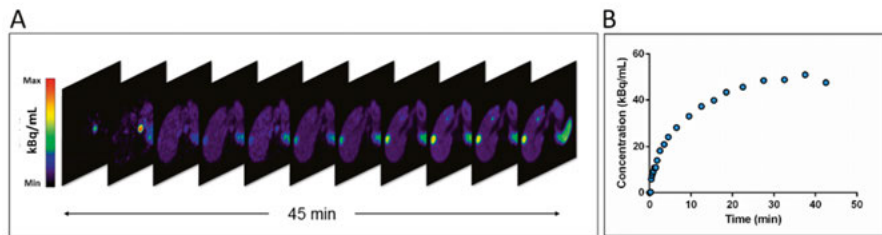


Figure 3. Dynamic PET scan showing images of a receptor tracer, ^{68}Ga -DOTATATE, during 45 min. p.i. of a bolus injection (A) and the corresponding TAC showing the activity concentration of the tracer over time in a tumor (B).

Compartment modeling

The tracers that are used in PET are developed to target physiological parameters such as receptor binding, metabolism, blood flow, and cell proliferation. The measured signal in the PET image consists of a mixture of several states of the tracer, such as tracer in the blood that has not yet entered the tissue, metabolized tracer, which still carries the radioactivity but is altered in its chemical form, and tracer within the tissue bound to the intended target, but also non-specifically bound and unbound tracer within the tissue of interest. With the intention of separating these states and estimating the parameter of

interest, kinetic modeling is applied to the dynamic PET images. Tracer kinetic modeling involves mathematical models describing the transport of tracer between plasma and different states or so-called compartments. The tracer kinetics can be estimated by compartment modeling. The most used compartment models are single- and two-tissue compartment models (1TCM and 2TCM) shown in Figure 4 A and B, respectively. In the compartment models, C_p represents the activity concentration in arterial plasma, C_{tissue} is the concentration of free, non-specific, and specific bound tracer in the tissue, $C_{free+ns}$ is the free and non-specific bound tracer in tissue, and C_{bound} represents the tracer specific bound to the target in tissue. The rate constants K_1 , k_2 , k_3 , and k_4 represent the exchange of tracer both between plasma and tissue and between different compartments. For tracers that are internalized in a tissue, the kinetics are irreversible, and the rate constant k_4 gets equal to zero (39,40). Since the tracer is injected into the blood and transferred to the tissue by the arterial plasma, the input concentration in the arterial plasma, which varies over time, must be measured. This can be accomplished by blood sampling from the patient's radial artery. The arterial whole-blood TAC can also be obtained by using the PET signal in the aorta when the aorta is in the field of view (FOV). This method is called image-derived input functions (IDIF). If the plasma-to-whole-blood ratio is constant during the time course of the PET scan, the input arterial plasma can be determined by multiplying the whole-blood signal from PET with the plasma-to-whole-blood ratio (41)

The compartment models can be described by first-order differential equations, and the parameters of interest can be derived using nonlinear regression (NLR) analysis. The most proper model will be chosen for the tracer of interest before analyzing the PET data (39,40). The solutions to these equations yield quantitative outcome parameters such as binding potential, distribution volume or net uptake rate. For an irreversible 2TCM ($k_4 = 0$ in Figure 4 B), the following differential equation can be used to describe the model:

$$\frac{dC_{free}(t)}{dt} = K_1 C_p(t) - (k_2 + k_3) C_{free}(t) \quad (2)$$

$$\frac{dC_{bound}(t)}{dt} = k_3 C_{free}(t) \quad (3)$$

The solution of these equations is as follows:

$$C_{PET}(t) = \frac{K_1 k_2}{k_2 + k_3} e^{-(k_2+k_3)t} \otimes C_p(t) + \frac{K_1 k_3}{k_2 + k_3} \otimes C_p(t) \quad (4)$$

in which $C_{PET}(t)$ represents the measured activity concentration in a VOI in the PET image. The internalization of the tracer is described by the second term on the right side of the equation; however, the parameter that is of interest is the net influx rate (K_i) representing the net influx of the tracers (39), or in receptor studies, representing both receptor density and the ability of the tracer to internalize in the tumors (42). The net uptake rate is defined as follows:

$$K_i = \frac{K_1 k_3}{k_2 + k_3} \quad (5)$$

By fitting Eq. 4 to the measured PET data using nonlinear regression (NLR), K_i can be determined (39).

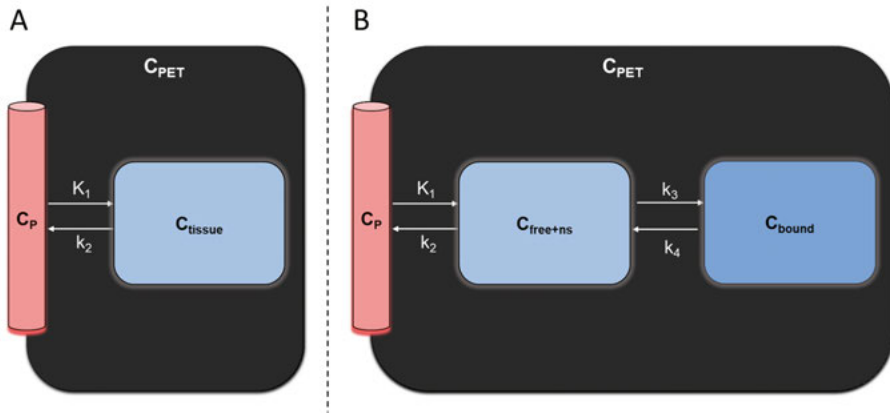


Figure 4. Schematic drawing of single-tissue (A) and two-tissue (B) compartmental model. The first compartment is the plasma concentration. In the single-tissue compartment model, the second compartment is the free, non-specific, and specific bound concentration in tissue (A). In the two-tissue compartment model, the second compartment is the free and non-specific bound concentration in a tissue, and the third is the specific bound concentration. The compartments are connected with rate constants (K_1 , k_2 , k_3 , and k_4).

Patlak plot

Graphical approaches have been proposed to transform the nonlinear compartment problem into a linear solution in which linear least square fit can be used to estimate parameters instead of NLR fit, so-called linearization. The Patlak plot (43) is the most commonly used graphical analysis for representing irreversible tracers ($k_4 = 0$) and estimating K_i . When using the Patlak plot, it is assumed that the reversible compartment, $C_{free+ns}$ (in the two-tissue compartment model, Figure 4 B) is in equilibrium with C_p . Hence, the ratio of tracer concentration in plasma and in the reversible compartment is stable. The system (Eq. 4) can then be described by the following equation:

$$C_{PET}(t) = K_i \int_0^t C_p(\tau) d\tau + v_e C_p(t) \quad (6)$$

Dividing both sides of Eq. 6 with the plasma time-activity concentration curve, $C_p(t)$, the system (Eq. 6) can now be described by a linear equation:

$$\frac{C_{PET}(t)}{C_p(t)} = K_i \frac{\int_0^t C_p(\tau) d\tau}{C_p(t)} + v_e \quad (7)$$

By plotting the left-hand side of Eq. 7 to the integral term divided with C_p (on the right-hand side of the equation), we obtain a linear graph where the slope represents the net influx rate K_i when equilibrium is reached, and the kinetics are irreversible (39).

Parametric images

The quantification mentioned so far has focused on estimating the parameter of interest (K_i) in VOIs (so-called VOI-based kinetic analysis). However, estimation of the parameter of interest can also be performed on a voxel level by constructing parametric images. Parametric images will visualize the physiological parameter of interest, such as K_i at the voxel level instead of the activity concentration, and allow for assessment of heterogeneity within the tissue. Because NLR for voxel-based parameter estimation is time consuming, linearization of the model can be used, such as Patlak plots or basis function methods of the irreversible 2TCM. The basis function method (BFM) is based on the linearization of Eq. 4 (the exponential term) by creating a library of possible solutions to the equation for a suitable range α of as follows:

$$BF = e^{-\alpha t} \otimes C_p(t) \quad (8)$$

where α is the sum of k_2 and k_3 . α is pre-calculated for a range of values for the exponential function. By convolving the plasma input function with the corresponding set of exponential functions, a set of basis functions, BF, can be obtained, which constructs a library of possible solutions. The irreversible 2TCM can now be rewritten as a linear combination of any one of the basis functions. The basis function resulting in the best fit to the data will be used (39).

Partial volume effect

The partial volume effect (PVE) is present both in SPECT and PET imaging and results in a difference between the measured (in the camera) and the true activity. PVE is a combination of two effects, limited spatial resolution, and image sampling. The finite spatial resolution of the system causes a three-dimensional blurring of the activity distribution. The measured activity in a hot lesion will be lower than it truly is, and a small object will appear larger but less radioactive than it truly is. Recovery is the ratio between the measured and true activity in small objects. The second effect, limited image sampling (voxel size), is due to the mismatch of the activity distribution between the voxel contour and that of the actual object contour. Since the activity distribution in SPECT and PET is sampled on a voxel grid, many voxels will include activity from different tissues, and the measured voxel will represent the average of the different tissue activity. Figure 5 illustrates the PVE (44).

Correction for PVE can be implemented both on the SPECT and PET data by performing phantom studies where recovery coefficients (RC) are calculated for spheres of varying size. The RC represents the relation between the measured and true activity or activity concentration (45).

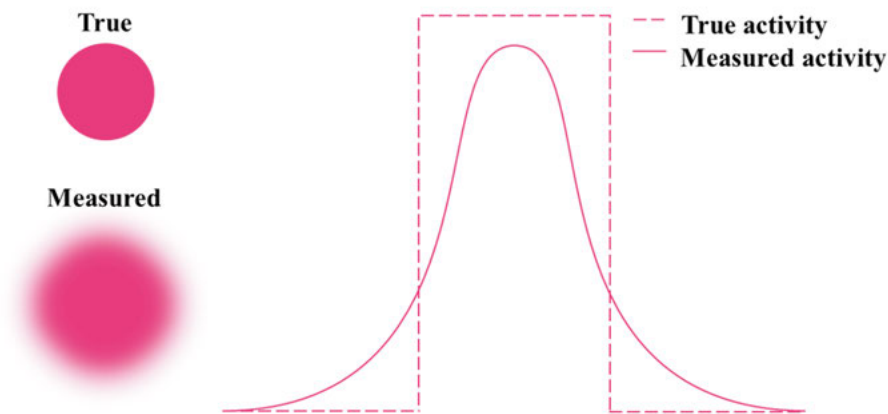


Figure 5. Schematic illustration of PVE in a hot lesion caused by limited spatial resolution. The measured lesion appears larger than the true lesion and the measured activity appears lower than the true activity, all due to PVE.

Treatment of NETs

First line treatment in localized NETs is surgery and is for many patients' curative, when the disease is detected at an early stage. Surgery is also performed for symptom relief, to prevent complications and to prolong life, even when the tumor has metastasized (46). Most NET patients are diagnosed at an

advanced stage (with lymph node and liver metastasis), and for patients with inoperable or metastasized tumors, cure is generally not possible and treatment merely palliative. In disseminated disease, unlabeled SSA constitutes a first-line treatment for low-grade NETs, usually administered as a long-acting release preparation, to decrease the hormonal symptoms and slow tumor growth (47). The unlabeled SSA does, however, not prolong survival in patients with small-intestinal NETs (48). Peptide receptor radionuclide therapy (PRRT) has shown to be effective as a therapeutic alternative and plays an increasingly important role in treatment of NET patients (49-59)

Peptide receptor radionuclide therapy

PRRT is a type of radionuclide therapy that involves systematic administration of a radiolabeled peptide (often an alpha- or beta-emitting radionuclide), targeting SSTR, overexpressed in NETs, with high affinity. The concept of PRRT is the same as SSA-imaging of NETs where the overexpressed receptors are targeted. However, instead of using a gamma-emitting radionuclide couple to the SSA via the chelator for imaging, radionuclides emitting charged particles (alpha and beta) with shorter ranges are used (60).

^{177}Lu is the most commonly used beta-emitting particle for PRRT, and ^{177}Lu -DOTATATE is the most used radiopharmaceutical for treating NET patients. PRRT with ^{177}Lu -DOTATATE has been used in patients with metastatic and advanced inoperable NETs since 2001 (59). In the prospective randomized controlled NETTER-1 trial, PRRT with ^{177}Lu -DOTATATE in combination with long-acting repeatable octreotide (LAR) showed favorable results in patients with advanced midgut NET, with longer progression-free survival (PFS) and higher response rate compared to high-dose octreotide LAR alone (61). Furthermore, PRRT with ^{177}Lu -DOTATATE also improved symptoms and quality of life (62).

Characteristics of ^{177}Lu

^{177}Lu is a low-energy beta-emitting radionuclide with a physical half-life of 6.73 days (60). It has three beta decay modes with energies (abundance %) of 47.7 (11.6), 111.7 (9.0), and 149.4 (79.4) keV, with a mean and max energy of approximately 133 and 498 keV. The low beta energy yields a maximum particle range of 2.2 mm in water with a mean range of 0.5 mm. The short range of beta particles emitted from ^{177}Lu decay affects cells in close proximity (typically tumor cells) and spares adjacent normal tissues. Since ^{177}Lu also emits gamma radiation with energies of 113 and 208 keV with an abundance of 6 and 11 %, respectively, ^{177}Lu can also be used for imaging (59). The characteristics of ^{177}Lu enable both imaging and therapy simultaneously and allow for performing dosimetry post-PRRT (60).

Treatment and imaging with ^{177}Lu -DOTATATE

^{177}Lu -DOTATE is administered as a fractionated treatment with a standard intravenous infusion of 7.4 GBq, repeated in four cycles with 8-12 weeks intervals (51,61,63). To prevent uptake in the kidneys, patients also receive a mixed amino acid solution administered concomitantly, starting ca 30 min pre-therapy. The standard protocol of four therapy cycles is based on a conservative safety margin for the organs at risk, which are the kidneys and bone marrow (20). The absorbed dose limits to the organs at risk in PRRT with ^{177}Lu -DOTATE are unknown, hence, the dose limit to the kidneys is adopted from external beam radiation therapy, and for the bone marrow from radioiodine therapy. According to these limits, the maximum acceptable absorbed dose to the kidneys is 23 Gy (64) and 2 Gy to the bone marrow (65), although in many patients higher absorbed doses to the kidneys have been achieved without high grade adverse effects, such as a biologically effective dose of 28 Gy or 40 Gy for patients without risk factors (66,67). With the same radiobiological basis as in external beam radiation therapy, the best PRRT result would be obtained when the treatment plan aims to deliver the highest (therapeutical effective) absorbed dose to the tumors while restricting the absorbed dose to the organs at risk below the threshold level for deterministic effects (68-70). Hence, the safety margin of only four treatment cycles leads to undertreatment in most patients.

Since ^{177}Lu emits gamma radiation, post-therapy imaging and dosimetry can be performed by SPECT imaging with a gamma camera. The images will visualize the tissue distribution of the radiopharmaceutical and enable quantification of normal organ and tumor uptake. However, for dosimetry, the total number of decays in the tissues and the kinetics of the radiopharmaceutical must be registered. Therefore, repeated SPECT in conjunction with computed tomography (SPECT/CT) imaging is performed to capture the dynamics of the uptake and elimination phase. In clinical practice, three or four time points are often chosen for imaging. When the activity within the ROI or VOI has been quantified at the different time points (by using a fixed threshold), a TAC is created, and the accumulated activity (or so-called time-integrated activity, TIA), which represents the total number of radioactive decays that occur in the region, can be estimated from the area under the curve by fitting a mono-exponential fit to the data (60,71).

Dosimetry

Estimating absorbed doses in organs at risk and tumors in PRRT is essential. The absorbed dose describes the amount of energy that has been deposited from ionizing radiation into a medium (such as an organ or tumor) and is given by the following equation:

$$D = \frac{d\bar{\epsilon}}{dm} \quad (9)$$

where $d\bar{\epsilon}$ is the mean energy imparted from ionizing radiation to a mass element dm . The standard method for absorbed dose calculations in internal dosimetry was specified by the committee on medical internal radiation dose (MIRD). Using the MIRD formalism, the mean absorbed dose D to a target tissue (r_T) over a defined dose integration period τ (usually set to infinity) after administration of the radiopharmaceutical is given as follows:

$$D(r_T, \tau) = \int_0^{\tau} \dot{D}(r_T, t) dt = \sum_{r_S} \tilde{A}(r_S, \tau) \cdot S(r_T \leftarrow r_S) \quad (10)$$

where $\tilde{A}(r_S, \tau)$ is the time-integrated activity (TIA) in the source tissue and $S(r_T \leftarrow r_S)$ is the pre-calculated dose conversion factor (S-factor), which represents the mean absorbed dose to target tissue r_T per decay in the source tissue r_S and depends on the properties of the radionuclide, age, and sex of the representative model and tissue of interest. The S-factors can be found in the MIRD scheme pamphlets or newer factors, called dose factors (DF), from OLINDA (organ level internal dose assessment) calculated with Monte Carlo simulations (71). Because the range of the beta particles is short (2.2 mm), it is assumed that there is only local absorption of the emitted beta particles ($r_T = r_S$), hence Eq. 10 can be simplified, and the mean absorbed dose can be rewritten as follows:

$$D = \tilde{A} \cdot S \quad (11)$$

where \tilde{A} is the time-integrated activity (TIA) in the target tissue and S is the dose conversion factor from MIRD (S-factor), including only self-dose (59).

Tumor dosimetry during PRRT with ^{177}Lu -DOTATATE is challenging because there are no S-factors for tumors. For tumor dosimetry, a different approach is therefore applied where a unit density sphere model is used. With the unit density sphere model (defined both in MIRD pamphlets (72) and OLINDA), the tumor self-dose can be calculated. The model assumes uniform activity distribution with spherical tumor shapes composed with unit density material. The dose factor will vary depending on the tumor size (73).

Pre-therapy dosimetry

SPECT imaging post PRRT with ^{177}Lu -DOTATATE at different time points enables post-therapy dosimetry. The calculated absorbed doses to the organs at risk and to the tumors are currently not routinely used for treatment planning. Instead, a fixed number of four cycles is administered to the patients. The accumulated data for PRRT with four cycles of 7.4 GBq ^{177}Lu -DOTATATE indicate that many patients are undertreated (68,74,75). In one study, more than > 50 % of the patients could receive more than four ^{177}Lu -DOTATATE cycles before reaching an absorbed dose of 23 Gy to the kidneys, and merely 20 % of the patients reached the 23 Gy absorbed dose threshold to the kidneys after four cycles of 7.4 GBq ^{177}Lu -DOTATATE. Patients who received as many cycles as possible up to the 23 Gy renal dose limit experienced significantly longer PFS than those who did not (33 versus 15 months), although not conclusive, because of the observational, non-controlled study design (68,74,75). In a simulated study, personalized PRRT based on the absorbed dose to the kidneys resulted in a 1.47-fold higher tumor-absorbed dose, which could have led to increased therapy response (75). However, increased response has not yet been demonstrated in a prospective trial.

Even though there are limitations in determining absorbed doses based on SPECT, the absorbed dose estimates contribute to the treatment planning because the absorbed dose to the organs at risk is monitored, in order to not exceed the dose limits (70). Dosimetry should optimally be performed individually for each patient. If dosimetry calculations were performed pre-therapy, as in external beam radiation therapy (dose planning), and as stated in the European Council directive, 2013/59/ Euroatom, (76), pre-therapy dosimetry could be used to individually plan PRRT and post-therapy dosimetry could be used to verify the plan. It is important to adopt strategies for PRRT that are in analogy with those for external beam radiotherapy, involving planning and verification of the absorbed dose both to tumors and organs at risk, to optimize the treatment individually for each patient (60). Since the absorbed doses not only depend on the amount of given radioactivity, but also on the kinetics of the radiopharmaceutical in the individual patient, an identical approach, as in external beam radiation therapy, is not possible in PRRT with ^{177}Lu -DOTATATE. Instead, a theranostic approach could be used for pre-therapy dosimetry, where a surrogate of the therapeutic radiopharmaceutical is used, for example ^{68}Ga -DOTATATE (77,78). Using a surrogate would allow pre-therapy dose planning and verification. Each treatment could be tailored individually for each patient, thus avoiding under- or overtreatment.

Treatment follow up of NETs

In parallel with the increasing use of ^{18}F -FDG PET/CT for therapy monitoring in conventional oncology, this application has also been suggested for NETs. Most NETs, however, show low proliferation and low metabolic activity and are therefore generally not ^{18}F -FDG avid (79). As an alternative, ^{68}Ga -DOTATOC and ^{68}Ga -DOTATATE have been suggested as a tool for evaluating therapy response in NET patients since most NETs express SSTRs (29,80,81), and SUV has been proposed as a marker of SSTR density. However, changes in tumor SUV during PET/CT with ^{68}Ga -DOTATOC or ^{68}Ga -DOTATATE have not been found to correlate reliably with the patient outcome (80-84). The difficulties in applying static tumor uptake measurements could partly be explained by the results in a study by Velikyan et al. (29). In that work, K_i , assumed to reflect SSTR density more accurately than SUV, was estimated based on dynamic PET images. It was found that SUV saturated to a static value for K_i ($> 0.02 \text{ mL/cm}^3/\text{min}$) for ^{68}Ga -DOTATOC and ^{68}Ga -DOTATATE, especially at higher SUVs (>20). Since SUV does not appear to reflect SSTR density for tumors with high receptor expression, K_i may therefore be a more adequate measure to reflect the tumor SSTR density than SUV.

Aims of the thesis

The general aim of this thesis was to develop novel methods in theranostic, where quantitative imaging with ^{68}Ga -DOTATATE/ ^{68}Ga -DOTATOC PET is used for optimizing PRRT with ^{177}Lu -DOTATATE for patients with NETs

More specifically, the aim of each study was the following:

Paper I

To investigate the tumor-absorbed dose–response relationship for PNETs treated with PRRT using ^{177}Lu -DOTATATE.

Paper II

To evaluate methods for computation of parametric K_i images compared to a VOI-based method and to explore the conditions for lesion detection in K_i images by assessing the image contrast in terms of tumor-to-liver ratios compared to those in static SUV images for ^{68}Ga -DOTATOC and ^{68}Ga -DOTATATE.

Paper III

To evaluate the relation between tumor-to-blood ratio (TBR) and K_i for patients undergoing PET/CT imaging with ^{68}Ga -DOTATOC and ^{68}Ga -DOTATATE.

Paper IV

To evaluate the time-dependent extended effect of receptor depletion and recirculation (7 h) of a single intravenous dose of 400 μg short-acting octreotide on tumor versus normal tissue uptake of ^{68}Ga -DOTATOC in SI-NET patients.

Paper V

To compare tumor uptake and kinetics of ^{68}Ga -DOTATATE with ^{177}Lu -DOTATATE by performing dynamic or serial static scans with both radiopharmaceuticals in the same patients.

Material and methods

Study population

Patients diagnosed with locally advanced and disseminated NETs, confirmed by histopathology, were included in this thesis. Paper I included twenty-four PNET patients who had undergone full treatment of PRRT with ^{177}Lu -DOTATATE. Paper II, III, and V included ten, twenty-two, and six patients with various NETs. Paper III included patients from both paper II and V. In Paper V, the included patients were planned for PRRT with ^{177}Lu -DOTATATE. Paper IV included four SI-NET patients who were progressing on long-acting SSA and who were planned for PRRT.

Data acquisition

Paper I

Patients included in Paper I had undergone 2-6 cycles of PRRT with ^{177}Lu -DOTATATE, and the individual number of cycles was based on the estimated absorbed doses to the kidneys and bone marrow. Most patients were infused with 7.4 GBq ^{177}Lu -DOTATATE at each cycle. For tumor-absorbed-dose estimations, at the first and third (or fourth) therapy cycle, serial SPECT/CT images were acquired 24, 96, and 168 h p.i. During intermediate therapy cycles, only a single SPECT/CT image was acquired 24 h p.i. Images were acquired on an Infinia Hawkeye SPECT/CT system (GE Healthcare) with MEGP collimators. The SPECT images were acquired using a 20 % energy window around the 208.4 keV energy peak with 120 frames á 30 s per frame. For evaluation of tumor response, clinical routine CT of the thorax and abdomen was performed pre-therapy, between cycles and post-therapy.

In Paper I, a phantom measurement was also performed for PVE correction. Six hollow spheres in a NEMA IQ phantom were filled with ^{177}Lu -DOTATATE and scanned in the same SPECT/CT scanner using the same imaging parameters as for patients.

Paper II & III

Patients in Paper II underwent a dynamic PET/CT examination after a bolus injection of ^{68}Ga -DOTATOC and ^{68}Ga -DOTATATE, on consecutive days. The same patients were included in Paper III along with a number of patients that underwent dynamic PET/CT examination with either ^{68}Ga -DOTATOC or ^{68}Ga -DOTATATE. In Paper II, the patients were scanned on a Discovery ST-PET/CT scanner (GE Healthcare). In Paper III, the patients were examined either on Discovery ST, Discover IQ, or Discovery MI (GE Healthcare). Dynamic scans started simultaneously with the intravenous injection of the tracers and was acquired during 45 min with 22 time frames with varying lengths (6x10, 3x20, 3x60, 5x180, 5x300 s). All patients included in Paper II also underwent whole-body PET/CT ca one h p.i, and venous blood samples were collected to assess whole-blood and plasma activity concentration.

Paper IV

All patients in paper IV underwent a baseline PET/CT (whole-body) with ^{68}Ga -DOTATOC, 1–3.5 months pre-study day (WB 0). On study day, patients were injected with a single intravenous infusion of 400 μg octreotide followed by three serial, dynamic PET/CT examinations (in sessions) at time 0 (1st dynamic scan), 3 h (2nd dynamic scan) and 6 h (3rd dynamic scan), starting simultaneously with intravenous injection of ^{68}Ga -DOTATOC. Each dynamic scan consisted of 45 min with 22 time frames (6x10, 3x20, 3x60, 5x180, 5x300 s). After each dynamic scan, three whole-body PET/CT images were acquired at time 1 h (WB 1), 4 h (WB 2), and 7 h (WB 3). Immediately, before the second and third dynamic scans, a 5-min static acquisition of the patients' upper abdomen was acquired to account for the remaining activity. All PET/CT examinations were performed on a Discovery MI PET/CT scanner. The patients in the study also underwent one cycle of PRRT with ^{177}Lu -DOTATATE (7.4 GBq) the day after the dynamic PET/CT examinations. An overview of the study design in Paper IV is presented in Figure 6.

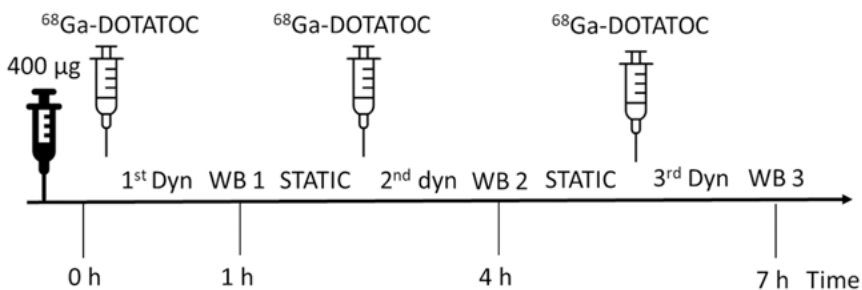


Figure 6. Schematic overview of study design. Baseline PET/CT was acquired pre-study, and PRRT with ^{177}Lu -DOTATATE was performed a period post study day.

Paper V

The patients received a bolus injection of ^{177}Lu -DOTATE with a low peptide dose (low-dose ^{177}Lu -DOTATATE) and underwent serial SPECT/CT examinations at 0.3, 0.7, 1, 2, 4, 24, and 96 h p.i in Paper V. Serial blood sampling was also performed to assess whole-blood and plasma activity concentrations. The day after (after the 24 h SPECT/CT scan), a dynamic, 45 min PET/CT scan with 22-time frames (6x10, 3x20, 3x60, 5x180, 5x300 s), was acquired, starting simultaneously with the ^{68}Ga -DOTATATE injection. Whole-body PET/CT scans were also performed 1 and 2 h p.i. Similar peptide dose was administered in the ^{68}Ga -DOTATATE ($17 \pm 4 \mu\text{g}$) and in the low-dose ^{177}Lu -DOTATATE ($17 \pm 3 \mu\text{g}$) preparations. The week after, all patients underwent their first PRRT cycle, 7.4 GBq ^{177}Lu -DOTATATE, with a high peptide dose of $254 \pm 45 \mu\text{g}$ (high-dose ^{177}Lu -DOTATATE) and serial SPECT/CT scans were acquired at 24, 96, and 168 h p.i. During PRRT, patients also received a mix of amino acid solution for kidney protection.

All SPECT/CT examinations were performed on a Discovery 670 PRO scanner (GE Healthcare) with MEGP collimators. A 20 % energy window was applied around the 208.4 keV energy peak. During low-dose ^{177}Lu -DOTATATE images with 60 or 120 frames during early and late time interval, respectively á 30 s per frame. During high-dose ^{177}Lu -DOTATATE, images were acquired with 120 frames á 30 s per frame. The PET/CT examinations were either performed on Discovery ST, Discovery IQ, or Discovery MI. The time duration of the dynamic images was 45 min with 22 time frames (6x10, 3x20, 3x60, 5x180, 5x300 s).

Overview of the study design in Paper V is presented in Figure 7.

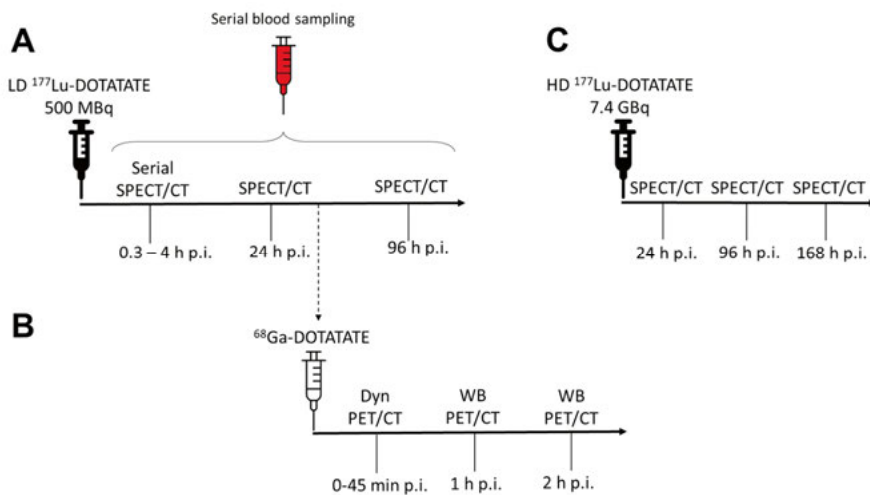


Figure 7. Schematic overview of study design. Low-dose (LD) ^{177}Lu -DOTATATE (A) was followed by dynamic and whole-body PET/CT scans with ^{68}Ga -DOTATATE (B). PRRT with high-dose (HD) ^{177}Lu -DOTATATE was performed ca week after day 1 (C).

Data analysis

Volume definition

The SPECT/CT examinations (clinical and phantom) in Paper I were analyzed on a Hermes workstation (Hybrid PDR, version 1.4B, Hermes medical solutions), and tumors (and phantom spheres) were delineated using an automated threshold of 42% isocontour VOI. In Paper V, the SPECT/CT images from low-dose and high-dose ^{177}Lu -DOTATATE were analyzed using the NEDPAS software (VU University Medical Centre, Amsterdam), and tumors were delineated by applying a 50 % isocontour threshold VOI. In Paper I, only tumors larger than 2.2 cm in diameter at any time during the treatment was included and a subgroup of tumors larger than 4 cm in diameter was also analyzed to avoid PVE effects. In Paper V, also only tumors with a diameter larger than 2.2 cm were included.

All PET/CT examinations in Paper II and III were analyzed using NEDPAS. For PET/CT examinations in paper IV, Hermes (Hybrid viewer PDR, version 5.1.1, Hermes Medical Solutions) was used and only tumors larger than 1 cm in diameter were included. Tumors were delineated in all PET/CT examinations by applying a 50% isocontour threshold VOI. In Paper II, a subsample of healthy liver was delineated in whole-body PET images using a 20 mL spherical VOI. Tumor and subsample of healthy liver were also delineated in parametric K_i images in Paper II using NEDPAS (with the same threshold and VOI size). In paper V, samples of normal organs (liver, left and right kidney, spleen, pancreas and bone marrow) were delineated using a spherical VOI with a diameter of 1.5 cm. A spherical VOI of 1 cm in diameter was also placed in the left ventricle of the heart.

In Paper II and VI, the descending aorta was delineated by placing a 1 cm diameter VOI in the lumen, and in Papers III and IV, a 70 % isocontour was applied instead.

Dosimetry and best response (I)

Tumor-absorbed dose calculations rely on sequential SPECT/CT images acquired at 24, 96, and 168 h p.i. of PRRT with ^{177}Lu -DOTATATE and were performed both for complete and intermediate dosimetry in Paper I. For dosimetric evaluation, the MIRD scheme was used (Eq. 11). However, instead of using the time-integrated activity \tilde{A} , the time-integrated-activity concentration, \tilde{C} , was determined; hence the activity concentration was used instead of the activity. The activity concentration was calculated for each SPECT scanning timepoint and corrected for PVE using recovery coefficients determined from phantom studies. The time-integrated-activity concentration was calculated as the area under the curve of a single exponential fit, and the following equation was used for absorbed dose calculations during complete dosimetry:

$$D = \tilde{C} \cdot ACDF \quad (12)$$

ACDF is the activity concentration dose factor, calculated as the dose factor (DF) for a 10 g sphere taken from OLINDA/EXM 1.1 multiplied by the weight of the sphere. An illustration of steps during complete dosimetry is presented in Figure 8. For intermediate dosimetry, which was performed at intermediate therapy cycles, the single-timepoint SPECT scanning was used, and the effective half-life from previous complete dosimetry was used; hence the effective half-life was assumed to be unchanged between complete and intermediate dosimetry. PVE correction was also performed during intermediate dosimetry calculations.

Tumor shrinkage, or best response, recorded from start of treatment until disease progression or recurrence, was determined according to response evaluation criteria in solid tumors (RECIST 1.1) by measuring the tumor diameters at CT scans acquired pre-treatment and at serial CT scans during follow-up.

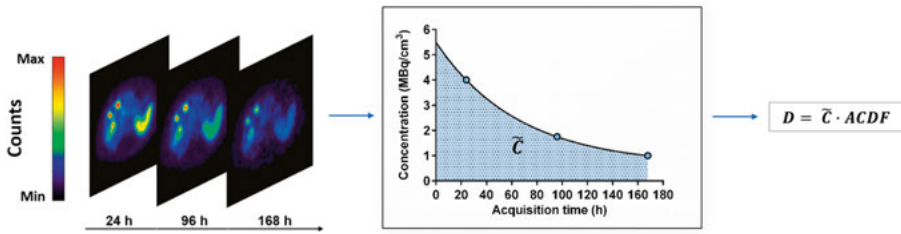


Figure 8. Schematic illustration of absorbed-dose calculations during complete dosimetry post-PRRT with ^{177}Lu -DOTATATE.

Kinetic analysis (II-V)

In Paper II, the net influx rate, K_i , for ^{68}Ga -DOTATOC and ^{68}Ga -DOTATATE, was determined by nonlinear regression of the irreversible two-tissue compartment model 2TCM (VOI-based method). Parametric K_i images were also computed in Paper II using a BFM implementation of the irreversible 2TCM and the Patlak method. The Patlak method was applied to the dynamic PET data, 15-45 min p.i. K_i from parametric images was compared to K_i obtained from the VOI-based method. In Papers III and IV, the Patlak method was used to determine K_i for ^{68}Ga -DOTATOC and ^{68}Ga -DOTATATE (15-45 min p.i.). In Paper V, K_i was determined for ^{68}Ga -DOTATATE and low-dose ^{177}Lu -DOTATATE both by nonlinear regression of the irreversible two-tissue compartment model with a loss parameter ($2T3k_{\text{Loss}}$) and by the Patlak method. For ^{68}Ga -DOTATATE, the Patlak method was applied to the 15-45 min p.i. dynamic data and for ^{177}Lu -

DOTATAE, for early (0–100 min p.i.) and late (>100 min p.i.) time interval. In Paper V, simultaneous estimation method fits (SIME) of ^{68}Ga -DOTATATE and low-dose ^{177}Lu -DOTATATE were also performed for $2T3k_{\text{Loss}}$ to determine K_i (K_i -SIME). For SIME, all the parameters were forced to be equal for both tracers, and a fitted recovery parameter was added to account for limited recovery in SPECT compared to PET.

For kinetic analysis of the PET data, the image-derived input function was calculated by multiplying the arterial time-activity concentration curve (uptake in the descending aorta over time) multiplied with a fixed plasma-to-whole-blood ratio. For the low-dose ^{177}Lu -DOTATATE data in paper V, the SPECT input function was based on serial blood samples.

Statistical analysis

All statistical analyses were performed using GraphPad Prism, GraphPad Software, Inc.

In **Paper I**, the square of the Pearson correlation coefficient was determined to evaluate the relation between the absorbed dose and tumor response both for tumors larger than 2.2 cm and 4 cm in diameter.

The agreement and correlation between VOI and parametric-based K_i values in **paper II** were determined using Pearson correlation and Deming regression.

In **Paper III**, blood SUV was compared between high (>0.2) and low (<0.2) K_i using the Mann-Whitney test. Linear regression and square of Pearson correlation (R^2) were used to evaluate the relationship between K_i and TBR and compared with the relation between K_i and SUV. Comparison of K_i , tumor SUV, and TBR between ^{68}Ga -DOTATOC and ^{68}Ga -DOTATATE was performed using Deming regression, the square of Pearson correlation, and Wilcoxon matched pairs test.

Tumor, organ, and whole-blood SUV (and normalized SUV) were compared between all whole-body images in **Paper IV**, using Wilcoxon matched-pairs test. The same test was performed for the three dynamic PET scans for K_i . The relationship between K_i and TBR was compared with the relationship between K_i and SUV and was evaluated using linear regression and the square of Pearson correlation.

In **Paper V**, to evaluate the agreement and difference in the relationship between ^{68}Ga -DOTATATE and low-dose ^{177}Lu -DOTATATE, Spearman correlation, Deming regression, and Wilcoxon matched-pairs signed rank test ($P<0.05$) were performed, respectively. This was also performed for high-dose and low-dose ^{177}Lu -DOTATATE in terms of SUV for tumors and whole-blood. To investigate the K_i relation, wherein K_i was derived from either the compartment models or the Patlak method, the same statistical analysis was applied.

For all tests, the significance level was set to a P value of less than 0.05.

Results

Paper I

Recovery coefficients were calculated for various sphere sizes in the NEMA IQ phantom to correct for PVE. The recovery coefficient depends on the sphere size and becomes lower with decreasing sphere diameter. For spheres smaller than 2.2 cm in diameter the recovery is less than 50 % (Figure 9 A). For spheres larger than 2.2 cm the measured diameters were in good agreement with the true diameter, whereas for spheres smaller than 2.2 cm, there was a severe overestimation of the measured diameter (Figure 9 B); hence tumors with a diameter smaller than 2.2 cm were excluded from the study.

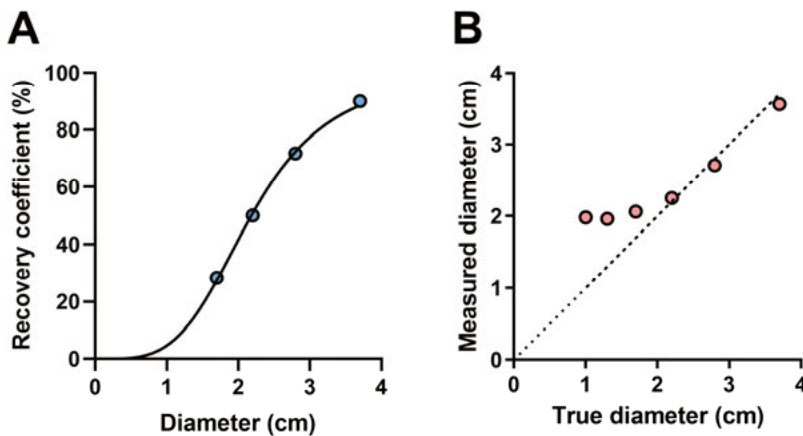


Figure 9. Recovery coefficient as a function of sphere diameter (A) and comparison between the true and measured diameters of the spheres (B) in the NEMA IQ phantom. The solid line represents 2 parameters sigmoid fit (A) and dashed line, line of identity (B).

For PNETs a clear correlation was found between tumor-absorbed dose and tumor reduction until best response, with a square of Pearson correlation of 0.64 and 0.91 for tumors larger than 2.2 and 4 cm in diameter, respectively.

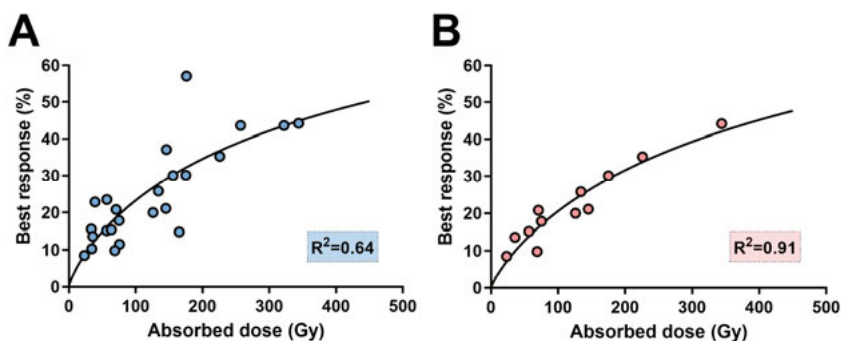


Figure 10. Tumor-absorbed dose relation (until best response) for PNETs treated with ^{177}Lu -DOTATATE in tumors larger than 2.2 cm (A) and 4 cm (B), respectively. The solid line represents 2 parameters sigmoid fit to the data.

Paper II

A linear and high correlation was found between VOI-based (NLR) and parametric-based (BFM and Patlak) K_i values both for ^{68}Ga -DOTATOC and ^{68}Ga -DOTATATE (Figure 11). The square of Pearson correlation (Deming regression slope) between NLR and BFM K_i values was 0.98 (0.81) and 0.97 (0.88) for ^{68}Ga -DOTATOC and ^{68}Ga -DOTATATE, respectively. For NLR and Patlak based K_i values, correlation (slope) was 0.95 (0.71) and 0.92 (0.74) for ^{68}Ga -DOTATOC and ^{68}Ga -DOTATATE, respectively.

K_i values between parametric-based BFM and Patlak were also compared, and a high correlation (square of Pearson correlation) was found for ^{68}Ga -DOTATOC (0.99) and ^{68}Ga -DOTATATE (0.98) with a Deming regression slope of 0.88 and 0.85, respectively.

The image contrast was evaluated in terms of tumor-to-liver ratio, and as seen in Figure 12, the contrast visually improves in the parametric images (BFM and Patlak) in comparison to the static whole-body PET image. The tumor-to-liver contrast was higher in the parametric K_i images (BFM and Patlak) than in the static whole-body images, and generally, the image contrast was higher for ^{68}Ga -DOTATATE than in ^{68}Ga -DOTATOC (Figure 13).

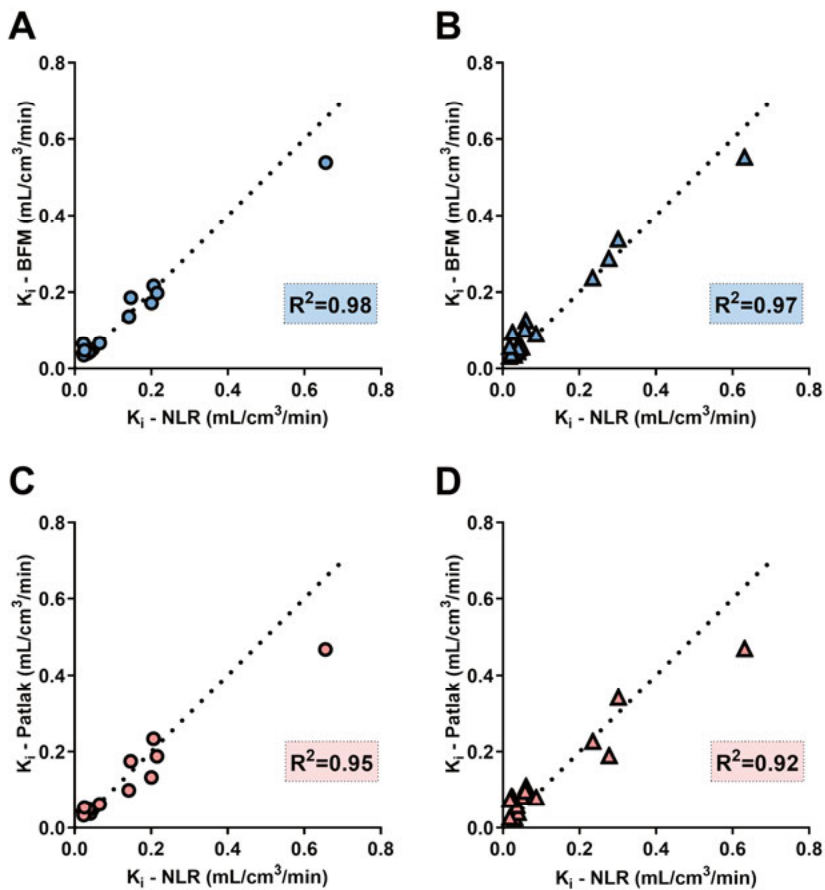


Figure 11. Relation between VOI-based (NLR) and parametric-based (BFM and Patlak) K_i values for ⁶⁸Ga-DOTATOC (A and C) and ⁶⁸Ga-DOTATATE (B and D).

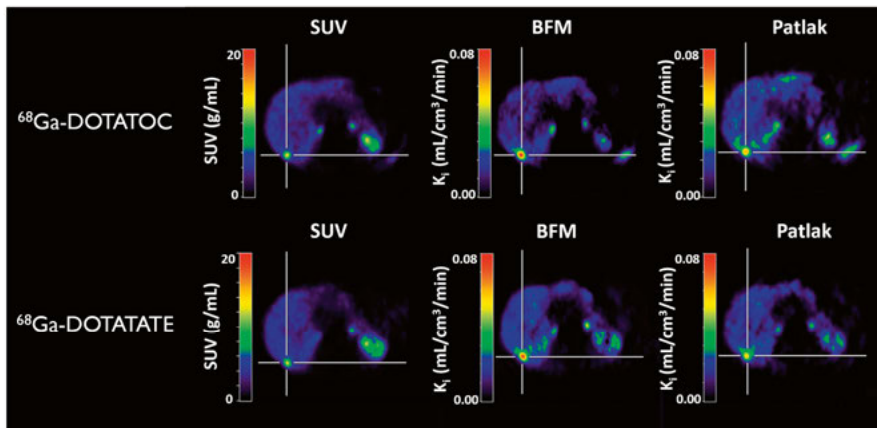


Figure 12. An illustration of representative transaxial SUV and K_i images of a patient's liver, with both ^{68}Ga -DOTATOC and ^{68}Ga -DOTATATE.

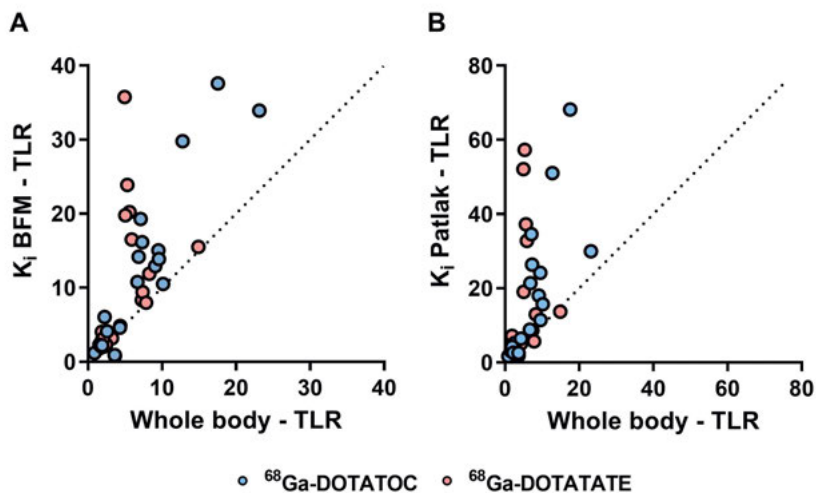


Figure 13. Comparison of tumor-to-liver ratio (TLR) between static whole-body PET images and parametric K_i images (BFM, A and Patlak, B) for ^{68}Ga -DOTATOC (blue dot) and ^{68}Ga -DOTATATE (red dot). TLR were 1.6 (blue dot, A), 2.0 (A, red dot), 2.3 (B, blue dot), and 3.0 (red dot) times higher in the parametric K_i images than in whole-body PET images.

Paper III

K_i and tumor-to-blood ratio (TBR) showed a linear relation, with a square of Pearson correlation of 0.98 and 0.98 for ^{68}Ga -DOTATOC and ^{68}Ga -DOTATATE, respectively (Figure 14 A and B). For the same tumors, a nonlinear relation was found between K_i and SUV (Figures 14 C and D).

For ^{68}Ga -DOTATOC, it was found that SUV in aortal blood (at 45 min p.i) was significantly lower in patients with high tumor K_i values (>0.2) than in those with low K_i values (<0.2), Figure 15 A. The difference was smaller for ^{68}Ga -DOTATATE, Figure 15 B. A comparison of K_i , tumor SUV, and TBR was performed between ^{68}Ga -DOTATOC and ^{68}Ga -DOTATATE. It was found that all three parameters were slightly higher for ^{68}Ga -DOTATATE than for ^{68}Ga -DOTATOC with a significant difference for TBR between the two tracers ($P=0.019$).

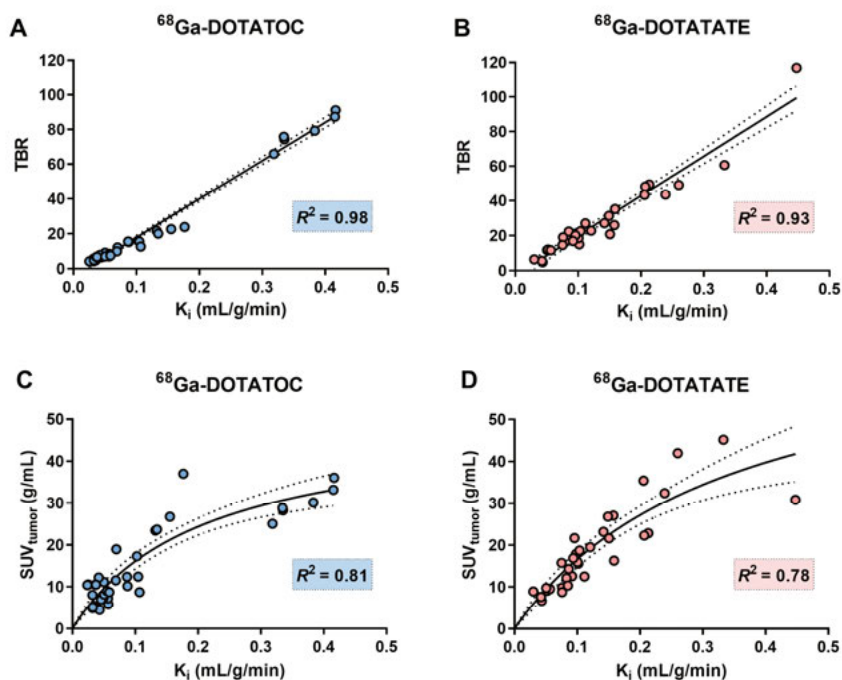


Figure 14. Correlation between K_i and TBR and K_i and SUV for ^{68}Ga -DOTATOC (A and C) and ^{68}Ga -DOTATATE (B and D). The solid line represents linear regression fit (A and B) and fit of a hyperbolic line (C and D), and the dashed line is the 95 % confidence band of the fits.

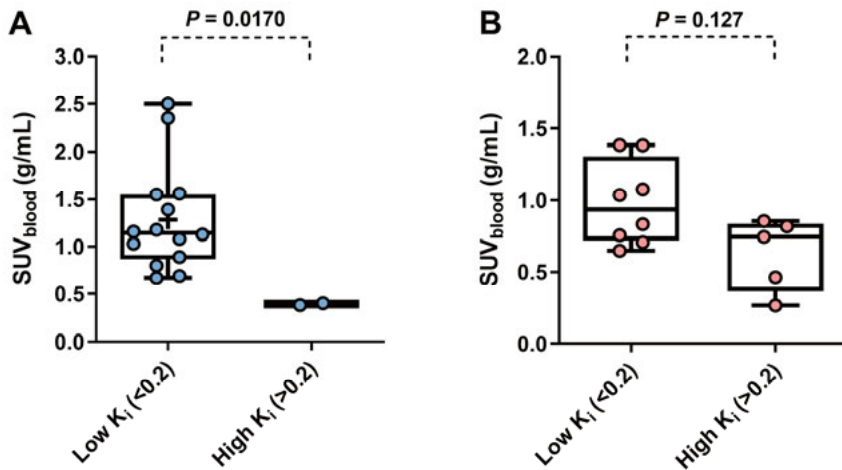


Figure 15. Box and whisker plot of SUV_{blood} at 40-45 min p.i. for $^{68}\text{Ga-DOTATOC}$ (A) and $^{68}\text{Ga-DOTATATE}$ (B) for high- and low K_i values. The box represents the median and the interquartile range, and the two lines are the whiskers presenting the highest and lowest observation.

Paper IV

Tumor SUV at whole-body PET (WB) 1, 2, and 3 were normalized against tumor SUV at baseline WB PET (WB 0). As seen in Figure 16, the uptake decreased from WB 0 to WB 1 (ratio <1) following intravenous injection of 400 μg octreotide, but with a subsequent recovery of the SSTR activity at WB 2 and WB 3 back to the baseline values, or even above, for some tumors at the last timepoint (WB 3). A significant increase ($P < 0.05$) was found in the normalized SUV between WB 1 and WB 2, between WB 1 and WB 3, and between WB 2 and WB 3. Thus, the normalized SUV returns to baseline levels at WB 2 and WB 3 (4 and 7 h p.i. of 400 μg octreotide), indicating a recovery from the receptor depletion between WB 0 and WB 1. The net influx rate, K_i , which was compared between the three dynamic scans (Figure 17), similarly showed a significant increase between the first and second and first and third ($P < 0.05$) scan, however not between the first and third scan ($P > 0.05$). K_i values were also compared to SUV and TBR and a linear correlation was found with the Pearson correlation (square) of 0.96 and 0.97, respectively. By contrast, in healthy organs, normalized SUV remained below one during all whole-body scans (WB 1, 2 and 3) in the liver, pancreas, and spleen (Figure 18 A-C). In contrast, in kidneys and bone marrow, some patients had normalized $SUV \geq 1$, with higher SUV in WB 1, 2, and 3 in comparison with SUV in WB 0 (Figure 18 D-F).

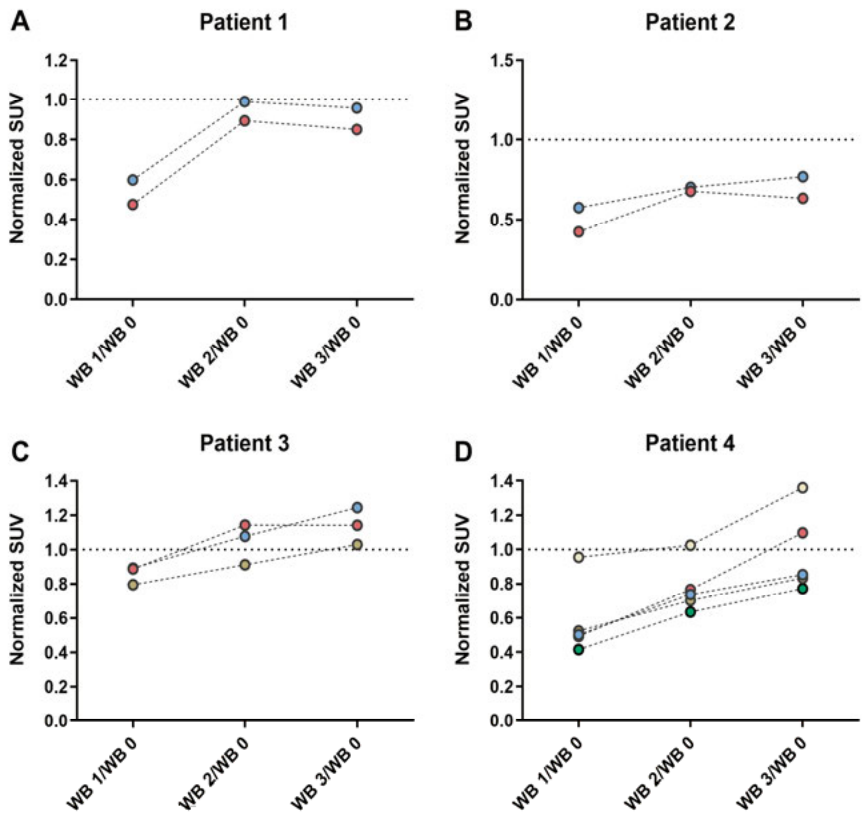


Figure 16. Normalized tumor SUV for patients in Paper IV, where SUV in whole-body (WB) 1, 2, and 3 is normalized against WB 0 (baseline scan).

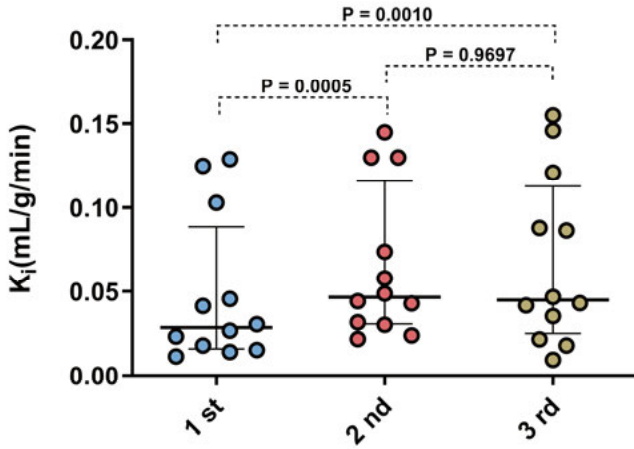


Figure 17. Scatter dot plots of K_i at the first, second, and third dynamic scan (0, 4, and 7 h). Between the first and the second dynamic scan, a significant increase was found in tumor K_i . This was also seen between the first and third dynamic scans but not between the second and third. Solid horizontal lines show median and interquartile range.

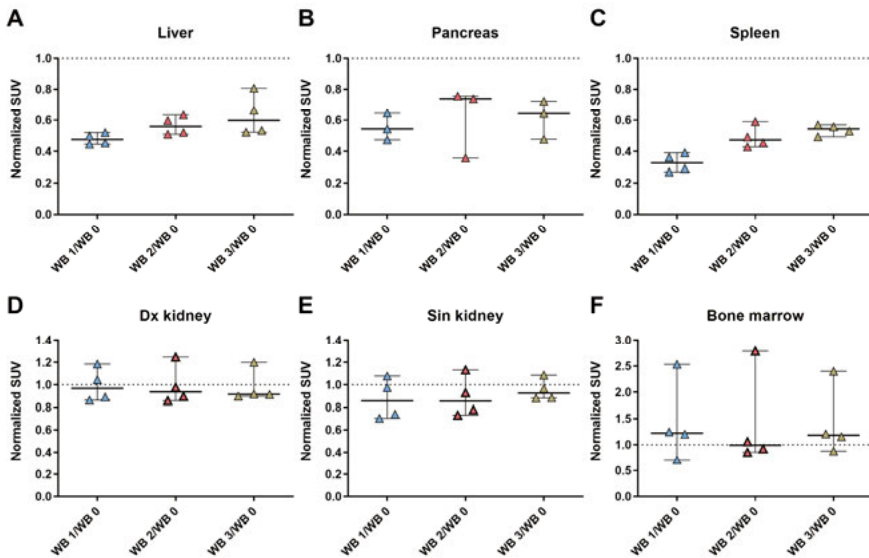


Figure 18. Scatter dot plots of normalized SUV in the liver (A), pancreas (B), spleen (C), dexter and sinister kidney (D and E), and bone marrow (F) where SUV in whole-body (WB) 1, 2 and 3 is normalized against SUV at WB 0 (baseline scan). Solid horizontal lines show median and interquartile range.

Paper V

In paper V, tumor SUV were significantly higher ($P < 0.05$) in ^{68}Ga -DOTATATE-PET than in low-dose ^{177}Lu -DOTATATE-SPECT (Figure 19 A), which agrees with the SUV images of the patients included in the study (Figure 20). The Spearman correlation was 0.75, and the Deming regression slope was 2.0 (Figure 19 A). Whole-blood SUV was lower in ^{68}Ga -DOTATATE than in low-dose ^{177}Lu -DOTATATE, resulting in a lower TBR for ^{68}Ga -DOTATATE than for low-dose ^{177}Lu -DOTATATE (Figure 19 B-C). The Spearman correlation was 0.43 and 0.53 for whole-blood SUV and TBR, with a Deming regression slope of 3.2 and 1.1, respectively (Figure 19 B-C). Tumor SUV was significantly higher in low-dose than in high-dose ^{177}Lu -DOTATATE ($P < 0.05$) and whole-blood SUV lower in high-dose ^{177}Lu -DOTATATE, resulting in a lower TBR for high-dose ^{177}Lu -DOTATATE (Figure 19 D-F). The Spearman correlation was 0.51, 0.93, and 0.49 for tumor and whole-blood SUV and TBR, with a Deming regression slope of 0.7, 2.0, and 0.6, respectively (Figure 19 D-F).

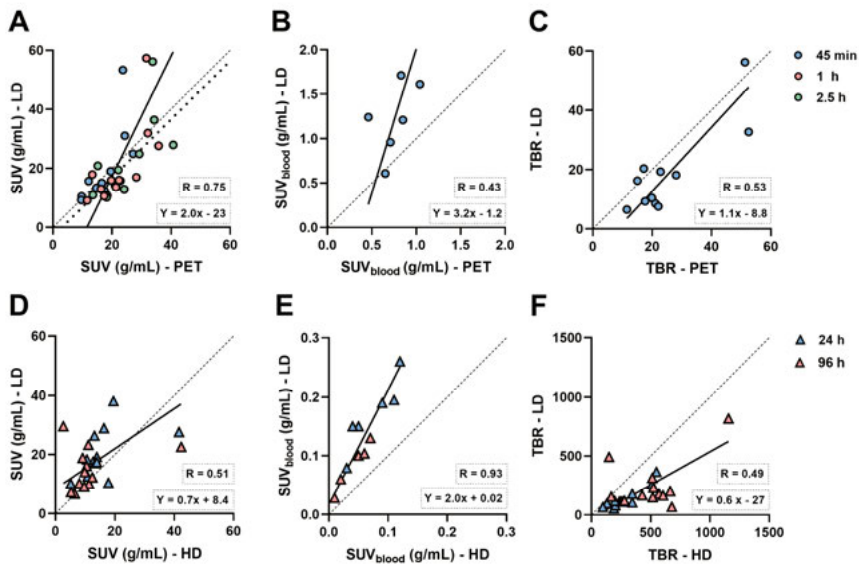


Figure 19. Tumor SUV (A), whole-blood SUV (B), and TBR (C) for ^{68}Ga -DOTATATE versus low-dose (LD) ^{177}Lu -DOTATATE and tumor SUV (D), whole-blood SUV (E), and TBR (F) for high-dose (HD) versus low-dose (LD) ^{177}Lu -DOTATATE. The blue, red, and green dots represent values from ^{68}Ga -DOTATATE and low-dose ^{177}Lu -DOTATATE images obtained 45 min, 1, and 2.5 h p.i., respectively. The blue and red triangles represent values from high-dose and low-dose ^{177}Lu -DOTATATE obtained 24 and 96 h p.i., respectively. The solid line represents the Deming regression fit to all data points, and the dashed line represents the line of identity. The dotted line (A) represents the Deming regression fit to the data, with a slope of 0.99, when one outlier tumor was excluded.

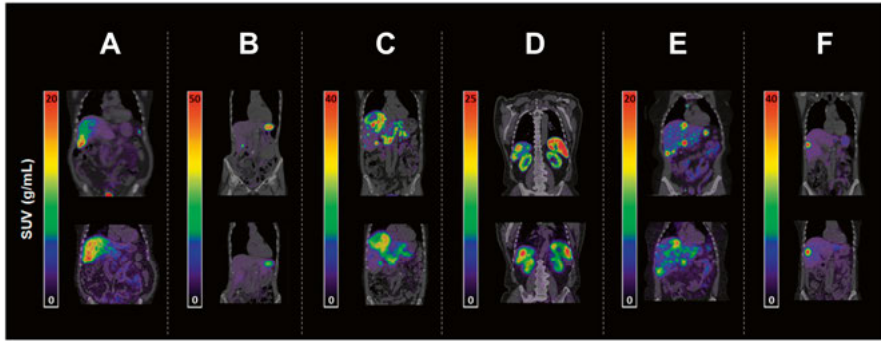


Figure 20. SUV images of ^{68}Ga -DOTATATE (top) and low-dose ^{177}Lu -DOTATATE (bottom) at approximately 1 h p.i. for all patients (A-F)

K_i from the $2T3k_{\text{Loss}}$ compartment model was compared between ^{68}Ga -DOTATATE and ^{177}Lu -DOTATATE (Figure 21 A). The Spearman correlation was 0.55, and the Deming regression slope was 0.093 between ^{68}Ga -DOTATATE and low-dose ^{177}Lu -DOTATATE. K_i from the $2T3k_{\text{Loss}}$ compartment model for ^{68}Ga -DOTATATE, and low-dose ^{177}Lu -DOTATATE was compared with K_i from the simultaneous estimation fit (SIME), (Figure 21 B). The Spearman correlation was 0.57 and 0.58 for ^{68}Ga -DOTATATE and low-dose ^{177}Lu -DOTATATE, respectively, and the Deming regression slope was 0.15 and 2.5.

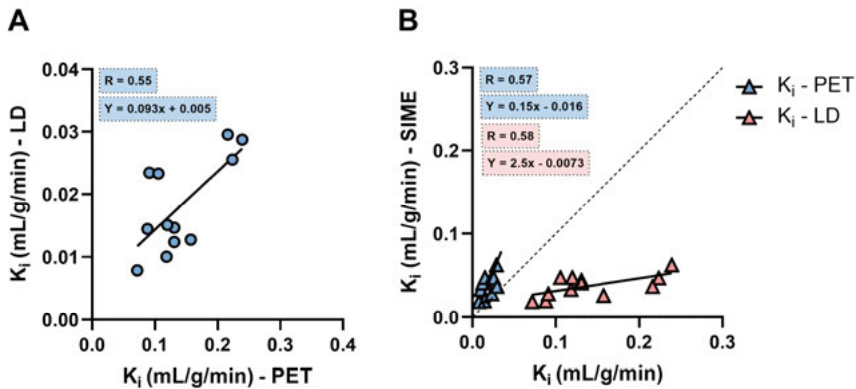


Figure 21. Net influx rate (K_i) in ^{68}Ga -DOTATATE (PET) versus low-dose ^{177}Lu -DOTATATE (LD) from the $2T3k_{\text{Loss}}$ compartment model (A). K_i in ^{68}Ga -DOTATATE (K_i - PET) and low-dose ^{177}Lu -DOTATATE (K_i - LD) from the $2T3k_{\text{Loss}}$ compartment model versus K_i from the simultaneous estimation fit of ^{68}Ga -DOTATATE and ^{177}Lu -DOTATATE (K_i - SIME), (B). The solid lines represent Deming regression fits, and the dashed line represents the line of identity.

Patlak analysis resulted in lower K_i in low-dose ^{177}Lu -DOTATATE than for ^{68}Ga -DOTATATE for both time intervals (Figure 22 A). With PVE correction applied on the low-dose ^{177}Lu -DOTATATE data, K_i increased, and the Spearman correlation increased from 0.73 to 0.90 and from 0.84 to 0.87 for early and late time intervals, respectively (Figure 22). The Deming regression slope increased from 0.60 to 0.83 and 0.11 to 0.18 for early and late time intervals, respectively. Patlak K_i for the early time interval for ^{68}Ga -DOTATATE and low-dose ^{177}Lu -DOTATATE becomes similar ($P>0.05$) with PVE correction (Figure 22 B); however, the same does not apply for the late time interval with PVE correction where Patlak K_i was still significantly higher ($P<0.05$) in ^{68}Ga -DOTATATE than in low-dose ^{177}Lu -DOTATATE.

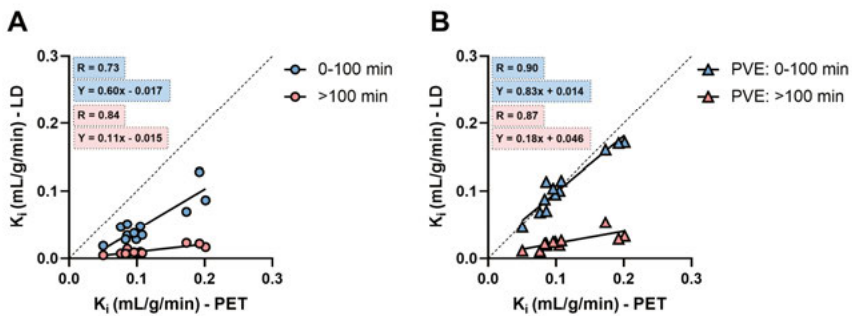


Figure 22. Early ($t = 0-100$ min) and late ($t > 100$ min) time interval Patlak K_i values for ^{68}Ga -DOTATATE (PET) versus low-dose ^{177}Lu -DOTATATE without (A) and with (B) PVE correction. The solid lines represent Deming regression fits, and the dashed line represents the line of identity.

Discussion

The first step in this thesis was to evaluate the relationship between tumor-absorbed dose and tumor reduction in patients with PNETs treated with ^{177}Lu -DOTATATE, as knowledge regarding this relationship is crucial for a better understanding of the important factors involved in the outcome of PRRT. In Paper I, a high correlation was found between tumor-absorbed dose and tumor reduction until best response. Hence, responding tumors have a higher absorbed dose. These results highlight the importance of delivering the highest possible dose to the tumors without exceeding the dose limits to organs at risk. Despite this absorbed dose-response relationship, some tumors with high absorbed dose showed little tumor reduction and vice versa. The main reason for this is thought to depend on factors affecting the specific tumor radiosensitivity, such as hypoxia and necrosis. Paper I had several limitations that could affect the absorbed dose calculations, such as assumption of unchanged effective half-life during intermediate treatment cycles, relying the absorbed dose calculations on a single image (24 h p.i.), limited spatial resolution, assumption of spherical tumor shape and homogenous uptake during PVE correction. Therefore, further work is needed to improve the accuracy of the absorbed dose calculations.

The NETTER-1 trial showed favorable PRRT results in patients with midgut NETs using the rigid treatment regime of four therapy cycles of 7.4 GBq ^{177}Lu -DOTATATE. In a meta-analysis by Kim et al., it was seen that the average disease control rate after treatment with PRRT was 82%. However, the response rates were much lower: 18–44% based on RECIST (85). Together with this paper, there is an increasing body of evidence that treatment outcome correlates with the delivered absorbed doses to the tumors and to organs at risk (86). These results indicate that more patients could benefit from more than four PRRT cycles and that the constrain of four therapy cycles (i.e., cohort-based “treatment planning”) can lead to over- or undertreatment due to large interpatient variability in organ distribution and consequently in radiation dose delivered to the tumors and healthy organs. A cohort-based approach should only be used when there are small biological variations within patients, which however not is the case for NET patients, who conversely constitute a very heterogenous group of patients (87,88). Paper I emphasized the importance of developing new methods to decrease the absorbed dose to the organs at risk, thereby increasing the tumor-absorbed dose. Hence. development

of methods for individualized radiotherapy planning is crucial. It is becoming more and more evident that PRRT should follow patient-specific treatment planning where the amount of administered activity and/or the number of PRRT cycles need to be estimated in order to achieve the desired absorbed doses (pre-treatment dosimetry). At least, post-therapy estimation of the absorbed dose needs to be performed for verification or post-therapy dosimetry. Thus, rather than using a “one-size-fits-all” approach, PRRT should be patient specific, in parallel to treatment planning applied for external beam radiotherapy (89,90).

The results from Paper II showed a high correlation between VOI and parametric-based K_i values and that the image contrast was higher in parametric K_i images than in SUV images both for ^{68}Ga -DOTATOC and ^{68}Ga -DOTATATE. Because early prediction of treatment response is essential to guide therapy, an imaging parameter to indicate a change of tumor SSTR density is required. To this end, changes in tumor SUV have been proposed but have, however, not been found to correlate with the treatment outcome. Velikyan et al. (42) previously showed that the relationship between K_i and SUV in NET is not linearly correlated, especially for higher SUV > 20–25. They therefore suggested that K_i may better reflect the tumor SSTR expression and that changes in K_i , rather than SUV, during treatment should be explored for therapy monitoring. However, in Paper II, it was found that k_3 was much higher than k_2 in patients with high K_i , indicating flow-limited delivery and a related underestimation of both K_i and SUV, which means that this cannot explain the divergence between K_i and SUV. In Paper III, our results further demonstrated that SUV does not correlate with K_i because of the low availability of tracer in the blood. When tumor SUV in static whole-body PET 1 h p.i. was normalized to SUV in the blood (TBR), a high linear correlation was found between TBR and K_i , both for ^{68}Ga -DOTATOC and ^{68}Ga -DOTATATE. This means that TBR constitutes a better tool than SUV to assess changes in SSTR expression for monitoring of treatment response. When SUV in blood was compared for patients with tumors with high and low K_i , respectively, a clear difference could be seen where high K_i yielded lower SUV in blood. K_i is not affected because plasma concentration is considered when estimating K_i in comparison with SUV, where the plasma concentration is not considered. Hence SUV is affected since the absolute amount of tracer taken up in tissue is limited by low plasma activity concentration, and will consequently be low in patients with high tumor SSTR density.

In paper IV, the kinetics of SSTRs depletion and reappearance in tumors (SI-NETs) was compared to that in normal organs, after a single intravenous injection of 400 μg octreotide. It was found that, compared to the baseline examination (WB 0), the SSTR expression in most tumors (and in liver, spleen and pancreas) dropped significantly following octreotide injection on the first whole body ^{68}Ga -DOTATOC PET/CT (WB 1). Over time (in WB 2 and 3), tumor SUV was however restored to the baseline level in almost all tumors;

but in the liver, spleen, and pancreas, only a partial recovery was seen at WB 3, the last point of measurement (7 h). These findings indicate a possible pathway for improvement of PRRT with ^{177}Lu -DOTATATE, by pre-injecting SSA 5-7 h pre-therapy. At the time of ^{177}Lu -DOTATATE administration, the receptors in the normal organs will still be depleted, in contrast to tumor SSTRs which have reappeared. Consequently, the relative amount of tumor SSTR available for binding will increase in relation to the normal tissue SSTRs. This can potentially increase the tumor-absorbed dose, and hence the response and treatment outcome, as discussed in Paper I. From a strict tissue uptake point of view, administration of additional peptide would not decrease the absorbed doses to kidney and bone marrow, except in patients with a large tumor load and high SSTR expression, where a high peptide amount may enhance the tumor sink effect and decrease the kidney and bone marrow dose. Tumor K_i was also determined in paper IV and was found to change over time in parallel with tumor SUV, which is not in agreement with our findings in Paper III and in the study by Velikyan et al. (42). In this paper (paper IV), where only SINET patients were included, a linear relation was found between K_i and SUV, even for tumors with high K_i (>0.2). One explanation for the deviating results could be the lower tumor burden of the patients in Paper IV in comparison to those in Paper III and in the study by Velikyan et al. Another explanation could be the higher amount of octreotide administered in Paper IV (400 μg) in comparison to the study by Velikyan et al. (20 μg), resulting in a higher tracer concentration in the blood because of depletion of binding sites in tumors and healthy organs. This will allow SUV to keep up with K_i even at high K_i values. Although paper IV shows convincing results, an obvious limitation of the study is the small number of patients. However, the consistent result across patients indicates that including more patients would not be likely to change the study outcome.

The results in Paper V demonstrated a high correlation and good agreement for tumor SUV and early K_i between ^{68}Ga -DOTATATE and low-dose ^{177}Lu -DOTATATE. TBR was for the majority of tumors lower for ^{68}Ga -DOTATATE than for low-dose ^{177}Lu -DOTATATE because of higher blood SUV in low-dose ^{177}Lu -DOTATATE than in ^{68}Ga -DOTATATE. For low-dose and high-dose ^{177}Lu -DOTATATE, slightly but significantly higher tumor SUV was observed for low-dose than for high-dose ^{177}Lu -DOTATATE, and higher TBR values were observed during high-dose ^{177}Lu -DOTATATE, suggesting that the low-dose ^{177}Lu -DOTATATE might not be used to represent high-dose ^{177}Lu -DOTATATE. A comparison of net influx rate, K_i , showed that the K_i from ^{68}Ga -DOTATATE (from $2T3k_{\text{Loss}}$) was lower than SIME and that ^{177}Lu -DOTATATE had higher K_i than SIME, suggesting that the kinetics of ^{68}Ga and low-dose ^{177}Lu -DOTATATE are dissimilar. However, for the early time interval, with PVE correction in the Patlak analyses, a high correlation and slope close to 1 was found for K_i between ^{68}Ga -DOTATATE and low-dose ^{177}Lu -DOTATATE. For the late time interval, a high correlation was also

observed; however, the slope was low (0.18), which might explain the weak correlation in K_i between ^{68}Ga -DOTATATE and low-dose ^{177}Lu -DOTATATE. These results show that the ^{68}Ga -DOTATATE data by itself does not contain enough information to fully predict ^{177}Lu -DOTATATE kinetics probably due to the loss of tracer at later time interval, which cannot be predicted from the 45 min PET scanning. The simultaneous estimation fit model (2T3k_{Loss} - SIME) showed that it is possible to describe both ^{68}Ga -DOTATATE and low-dose ^{177}Lu -DOTATATE kinetics with the same parameters. This was confirmed by the Patlak analysis in which the early behavior of ^{68}Ga -DOTATATE and low-dose ^{177}Lu -DOTATATE appears to be identical after PVE correction of the PET data. Notably, the late Patlak analysis of ^{177}Lu -DOTATATE shows an apparent nearly fivefold reduction in K_i , likely due to loss of ^{177}Lu from the tumor. As the reduction in K_i at late time interval seems to be rather consistent across tumors and patients, it may be possible to apply this information in predicting ^{177}Lu -DOTATATE kinetics, which will be the subject of further work.

A factor that could have affected the results in this paper is the absence of phantom-based PVE correction of the ^{68}Ga -DOTATATE data compared with the ^{177}Lu -DOTATATE data. However, this effect was minimized by excluding tumors smaller than 2.2 cm in diameter from the PET data. Hence, the absence of PVE correction was expected to be of minor consequence. Another limitation was that the VOIs were defined separately in the ^{68}Ga -DOTATATE and ^{177}Lu -DOTATATE images, respectively, resulting in differences in VOI size. The same threshold was however applied to minimize these differences.

Concluding remarks

This work yielded the following main findings:

In **Paper I**, a significant correlation was found between the tumor-absorbed dose until best response and tumor response in PNETs. The therapy outcome is better at higher absorbed doses in terms of tumor reduction. Hence, responding PNETs have higher absorbed doses than non-responding tumors.

In **Paper II**, a high correlation and agreement were found between the VOI and the two sets of parametric-based K_i values, validating the use of K_i at the voxel level for both ^{68}Ga -DOTATOC and ^{68}Ga -DOTATATE. K_i -value at the voxel level is desired since it provides information on tumor heterogeneity that is lost when average tumor K_i is measured. In addition, parametric images resulted in better tumor-to-liver contrast than standard whole-body images. Since most patients with NETs have metastases in the liver, the reduced background signal from the liver, facilitates tumor visualization.

In **Paper III**, for both tracers, a linear relation was found between K_i and TBR with a significant difference in $\text{SUV}_{\text{Blood}}$ between patients with high and low K_i values, respectively. The difference in $\text{SUV}_{\text{Blood}}$ explains the nonlinear correlation between K_i and SUV at higher K_i values. The results from this study can provide a therapy monitoring tool to use for early prediction of therapy response which is essential to guide tumor therapy and avoid unnecessary side effects and additional costs due to ineffective treatments.

In **Paper IV**, faster recycling of somatostatin receptors was found in tumors than in healthy organs. This knowledge opens the possibility of protecting normal tissue during PRRT with ^{177}Lu -DOTATATE by administering a single dose of cold peptide pre-PRRT. This may also improve the availability and uptake of ^{177}Lu -DOTATATE in tumor tissue.

In **Paper V**, a linear relation with good agreement was found between ^{68}Ga - and low-dose ^{177}Lu -DOTATATE (tumor SUV and early K_i) and between high and low-dose ^{177}Lu -DOTATATE (tumor SUV). However, the kinetics of ^{68}Ga -DOTATATE could not be used for predicting the kinetics of ^{177}Lu -DOTATATE during PRRT since the loss of tracer at later time points cannot solely be predicted from the PET scan.

Future perspectives

The future is bright for theranostics, where quantitative imaging with ^{68}Ga -DOTATATE and ^{68}Ga -DOTATOC-PET is used to optimize PRRT with ^{177}Lu -DOTATATE. In Paper IV a faster recycling of somatostatin receptors in tumors than in healthy organs was illustrated after pre-injection with a cold somatostatin analog. This knowledge opens the possibility of protecting normal tissue and improve the availability and uptake of ^{177}Lu -DOTATATE in tumors; therefore, in future studies, cold peptide should be administered pre-PRRT to test and verify this hypothesis. Given that the hypothesis holds true in the therapy situation, this would increase the tumor-absorbed dose, hence tumor response, and decrease the adverse effects from normal tissues.

The results of Paper V demonstrated an apparent near-fivefold reduction in K_i at late time interval in comparison to early time interval. As the reduction in K_i at late time interval seems to be rather consistent across tumors and patients, it may be possible to apply this information on the ^{68}Ga -DOTATATE-PET data for predicting ^{177}Lu -DOTATATE kinetics.

The results from Paper V also open the way for future studies with ^{68}Ga -DOTATATE as a surrogate for ^{177}Lu -DOTATATE, also comparing parameters such as SUV, TBR and K_i from ^{68}Ga -DOTATATE to tumor-absorbed doses from PRRT with ^{177}Lu -DOTATATE. Further, other tracers than ^{68}Ga -DOTATATE with longer half-life, such as ^{64}Cu -DOTATATE or ^{66}Ga -DOTATATE, could be used as a surrogate marker for pre-therapy dosimetry during PRRT with ^{177}Lu -DOTATATE. The results obtained in the present work may also be relevant to other theranostic combinations, such as with $^{68}\text{Ga}/^{177}\text{Lu}$ -PSMA (prostate-specific membrane antigen) in the treatment of metastasized prostate cancer and $^{68}\text{Ga}/^{177}\text{Lu}$ -FAPI (fibroblast-activation-protein inhibitors) for various types of cancers.

Populärvetenskaplig sammanfattning

Neuroendokrina tumörer (NET) är sällsynta och utgår från celler i det diffusa endokrina systemet fördelade i hela kroppen. NET uppstår oftast i mag-tarmkanalen, inklusive bukspottskörteln, samt i lunga och bronker. Den kliniska bilden av NET varierar mycket beroende på var den uppstår, p.g.a. olika lokala symptom, och att patienterna både kan ha och sakna symptomgivande hormonproduktion så som diarré och värmevallningar. Patienter med NET diagnostiseras ofta när tumören redan har metastaterats och då går sjukdomen inte länge kan bota med kirurgi. De allra flesta NET uttrycker somatostatinreceptorer på cellytan, vilket möjliggör användning av peptider (somatostatinanaloger) som binder till dessa receptorer som är märkta med en radioaktiv isotop, för både diagnostisering och intern strålbehandling. Standard avbildningsmetod för att diagnostisera patienter med NET är positronemissionstomografi tillsammans med skiktröntgen (PET/CT), som är en s.k. molekylär avbildningsmetod. Patienten injiceras med en somatostatinanalog (DOTATATE eller DOTATOC) som är märkt med den positronstrålande radioaktiva isotopen gallium-68 (^{68}Ga). ^{68}Ga -DOTATATE eller ^{68}Ga -DOTATOC söker sig till receptorerna som finns på tumörcellerna, och när ^{68}Ga sönderfaller via positronemission ger det upphov till emission av två fotoner som registreras av PET-kameran och möjliggör därmed avbildning av tumörupptaget. I PET-kameran kan man utföra både statiska mätningar för att få helkroppsbilder och dynamiska mätningar för att få en bildserie över tid. Från PET-bilderna kan man beräkna ett standardiserat upptagsvärde (SUV), vilket är en semikvantitativ parameter som ger en uppskattning av upptaget i framför allt tumörerna. Denna parameter brukar ofta användas för att utvärdera tumörrespons efter behandling. Från de dynamiska bildserierna kan man dessutom beräkna ett mer kvantitativt värde, K_i , som representerar både densiteten av somatostatinreceptorer och somatostatinanalogens förmåga att internaliseras i tumörcellerna. I tidigare studier där man har jämfört SUV och K_i har man funnit ett avtagande samband mellan dessa för höga K_i -värden.

Tumörernas höga uttryck av somatostatinreceptorer möjliggör behandling med månadsvisa injektioner av långverkande somatostatinanaloger som dämpar de hormonrelaterade symtomen och hämmar tumörtillväxten. Dessa injektioner förlänger tiden till progress av sjukdomen, men leder sällan till tumörminskning. Sedan 2001 används intern strålbehandling för patienter med

NET, s.k. peptidreceptorradionuklidterapi (PRRT), där DOTATATE märks med den radioaktiva isotopen Lutetium-177 (^{177}Lu). Vanligtvis behandlas patienter med fyra injektioner (cykler) av ^{177}Lu -DOTATATE, men på Akademiska sjukhuset i Uppsala har antalet behandlingar i stället baserats på den absorberade dosen till riskorganen (njurar och benmärg) som är känsliga för strålning. Behandlingen bygger på samma princip som vid PET-diagnostiken, men i detta fall är den radioaktiva isotopen en betastrålare, vilket ger en intern strålbehandling till tumören. Förutom betasönderfall så sker även gammasönderfall som ger upphov till emission av fotoner. Tack vare emissionen av dessa fotoner kan tre-dimensionella gammakamera-bilder (SPECT) erhållas som visar upptaget av ^{177}Lu -DOTATATE i patienten efter behandling.

Syftet med avhandlingen var att undersöka sambandet mellan absorberad tumördos och tumörkrympningen hos patienter med NET i bukspottskörteln efter PRRT med ^{177}Lu -DOTATATE. Syftet var även att utveckla nya metoder för att använda ^{68}Ga -DOTATOC och ^{68}Ga -DOTATATE för att optimera PRRT med ^{177}Lu -DOTATATE. I det första delarbetet fann vi en direkt relation mellan graden av tumörkrympningen och den absorberade dosen i tumörerna. Detta visar att ju fler behandlingscykler patienten kan erhålla, desto högre stråldos i tumörerna och desto effektivare tumörkrympning. I det andra och tredje delarbetet jämfördes två olika metoder för att bestämma K_i och dessutom jämfördes kontrasten mellan upptaget i tumör och lever för de två olika metoderna, både för ^{68}Ga -DOTATATE och ^{68}Ga -DOTATOC. Det avtagande sambandet mellan SUV och K_i , som tidigare studier visat för höga K_i värden, undersöktes också för att utvärdera om SUV är ett bra mått för att utvärdera tumörrespons efter behandling. Vi fann att båda metoderna gav liknande K_i värden, men att ena metoden gav högre kontrast mellan upptaget i tumör och lever. Vidare bekräftade vi det avtagande sambandet mellan SUV och K_i vid höga K_i värden och att detta var på grund av låg tillgänglighet av ^{68}Ga -DOTATATE och ^{68}Ga -DOTATOC i blodet. När tumörupptaget normaliseras till upptaget i blod (TBR) fann vi emellertid ett linjärt samband mellan TBR och K_i . Vår slutsats är därför att K_i eller TBR bör användas för att mäta tumörrespons efter behandling i stället för SUV. Det fjärde delarbetet utfördes för att utvärdera huruvida kall peptid (octreotid), som inte märkts med radioaktiva isotoper, injicerad innan patienten genomgår undersökning med ^{68}Ga -DOTATOC, har betydelse för tumör- och normalvävnadsupptaget. Vi fann att för-injektion av octreotid sänkte upptaget i normalvävnad, så som lever, mjälte och bukspottskörtel, och att tumörupptaget först sänktes men sedan återupprättades efter kort tid. Det öppnar upp möjligheten att vid PRRT skydda normalvävnaderna samt öka tillgängligheten av den radioaktivt märkta somatostatinanalogen till tumörerna genom för-injektion av octreotid några timmar innan behandlingen. Det femte och sista delarbetet gick ut på att jämföra kinetiken mellan ^{68}Ga -DOTATATE och ^{177}Lu -DOTATATE i syfte att kunna använda ^{68}Ga -DOTATATE-PET för dosimetri vid PRRT med ^{177}Lu -DOTATATE. Vi fann ett linjärt samband med god överensstämmelse i

tumörvävnad för SUV och K_i (tidig kinetik) mellan ^{68}Ga -DOTATATE och ^{177}Lu -DOTATATE, men kinetiken för ^{68}Ga -DOTATATE kunde inte användas för att förutsäga den sena kinetiken för ^{177}Lu -DOTATATE. Sammanfattningsvis visar kvantitativ PET-avbildning med ^{68}Ga -DOTATATE och ^{68}Ga -DOTATOC en stor potential både för utvärdering av terapi svar och för att optimera behandlingen av NET-patienter som behandlats med ^{177}Lu -DOTATATE.

Acknowledgement

My journey towards finalizing this thesis has been packed with fun and a lot of interesting challenges and I would like to take this opportunity to express my gratitude to all those who were present during this journey and forgive me if I missed mentioning someone.

First and foremost, I would like to express my deepest gratitude to my main supervisor, Mark Lubberink, for his support, motivation, and immense knowledge. You have been such an inspiration from the first day and this work would not have been possible without you!

I would also like to express my gratitude to my co-supervisors; Mattias Sandström, Anders Sundin and Irina Velikyan, for their engagement and valuable input. Special thanks to Mattias for introducing me to world of radionuclide therapy and for all your help related to this topic. Anders, thank you for your open attitude, for always being prepared to share your scientific skills and for your support in manuscript writing. Irina, thank you for interesting discussions and supportive manuscript suggestions which were insightful and always positive.

Thanks to all the co-authors who helped to improve the manuscripts, came with improving insight and opportunities to develop such a nice work. To all the staff at Nuclear medicine and PET-center for patient treatment and imaging. To my roomie, My and my “extra roomie”, Elin, for your endless positive support and interesting discussions. It would all be so boring without you! To all colleagues at the Department of Radiation Physics for pleasant company and interesting discussions. Especially, I want to thank Adrian and Charles. To all my colleagues at 14 B, especially Naresh, Marcos and Ali for never ending interesting and joyful discussions in the office and lunch-room. To Ulrike Garske, for handing me the valuable PNET-data, the first paper would not have been possible without your help! To Ulrika Jahn, for interesting discussions regarding tumor biology. Thanks to you I have more understanding about NET biology.

Thanks to my friend and family that have supported me on this journey. Especially, Mirna and Mladen, for helping and supporting me with studies and giving me mental support since I can remember. My sisters, Berna and Eylem, for their tremendous support, for always being there for me and for their mental support and help with household chores so that I could study and focus. My nieces; Ela, Dila, and Leah, for giving me joy and their love. My parents

for their endless support, encouragement, love and everlasting generosity since my childhood. My father for teaching me how important it is to be independent and for always believing in me and supporting me economically during my studies. My mother for believing in me, for always trying with different methods to improve my focus and for bringing be walnuts and raising every time I studied since I was a kid. Thank you for everything, I would not be who I am and where I am today without your support. I love you!

Lastly, my hubby, Bünyamin, words are not enough to express my love and gratitude to you. Thank you for your endless love and support no matter what and for bringing me down to earth and reminding me of the most important things in life. And my baby boy for giving everything a new meaning. I love you!

References

1. Hanahan D, Weinberg RA. The hallmarks of cancer. *Cell*. 2000;100:57-70.
2. Sun XX, Yu Q. Intra-tumor heterogeneity of cancer cells and its implications for cancer treatment. *Acta Pharmacol Sin*. 2015;36:1219-1227.
3. Shin SH, Bode AM, Dong Z. Precision medicine: the foundation of future cancer therapeutics. *NPJ Precis Oncol*. 2017;1:12.
4. Rindi G, Klimstra DS, Abedi-Ardekani B, et al. A common classification framework for neuroendocrine neoplasms: an International Agency for Research on Cancer (IARC) and World Health Organization (WHO) expert consensus proposal. *Mod Pathol*. 2018;31:1770-1786.
5. Nagtegaal ID, Odze RD, Klimstra D, et al. The 2019 WHO classification of tumours of the digestive system. *Histopathology*. 2020;76:182-188.
6. Modlin IM, Oberg K, Chung DC, et al. Gastroenteropancreatic neuroendocrine tumours. *Lancet Oncol*. 2008;9:61-72.
7. Modlin IM, Kidd M, Latich I, Zikusoka MN, Shapiro MD. Current status of gastrointestinal carcinoids. *Gastroenterology*. 2005;128:1717-1751.
8. Graham MM, Gu X, Ginader T, Breheny P, Sunderland JJ. (68)Ga-DOTATOC Imaging of Neuroendocrine Tumors: A Systematic Review and Metaanalysis. *J Nucl Med*. 2017;58:1452-1458.
9. Oberg K, Astrup L, Eriksson B, et al. Guidelines for the management of gastroenteropancreatic neuroendocrine tumours (including bronchopulmonary and thymic neoplasms). Part I-general overview. *Acta Oncol*. 2004;43:617-625.
10. Guilmette JM, Nosé V. Neoplasms of the Neuroendocrine Pancreas: An Update in the Classification, Definition, and Molecular Genetic Advances. *Adv Anat Pathol*. 2019;26:13-30.
11. Ito T, Igarashi H, Jensen RT. Pancreatic neuroendocrine tumors: clinical features, diagnosis and medical treatment: advances. *Best Pract Res Clin Gastroenterol*. 2012;26:737-753.
12. Cives M, Pelle E, Quaresmini D, Rizzo FM, Tucci M, Silvestris F. The Tumor Microenvironment in Neuroendocrine Tumors: Biology and Therapeutic Implications. *Neuroendocrinology*. 2019;109:83-99.
13. Kidd M, Modlin I, Öberg K. Towards a new classification of gastroenteropancreatic neuroendocrine neoplasms. *Nat Rev Clin Oncol*. 2016;13:691-705.
14. Yao JC, Hassan M, Phan A, et al. One hundred years after "carcinoid": epidemiology of and prognostic factors for neuroendocrine tumors in 35,825 cases in the United States. *J Clin Oncol*. 2008;26:3063-3072.
15. Krenning EP, Kwekkeboom DJ, Bakker WH, et al. Somatostatin receptor scintigraphy with [111In-DTPA-D-Phe1]- and [123I-Tyr3]-octreotide: the Rotterdam experience with more than 1000 patients. *Eur J Nucl Med*. 1993;20:716-731.
16. Hoyer D, Lübbert H, Bruns C. Molecular pharmacology of somatostatin receptors. *Naunyn-Schmiedeberg's Archives of Pharmacology*. 1994;350:441-453.

17. Patel Y. Molecular pharmacology of somatostatin receptor subtypes. *Journal of endocrinological investigation*. 1997;20:348-367.
18. Reubi JC. Peptide Receptors as Molecular Targets for Cancer Diagnosis and Therapy. *Endocrine Reviews*. 2003;24:389-427.
19. Patel YC. Somatostatin and Its Receptor Family. *Frontiers in Neuroendocrinology*. 1999;20:157-198.
20. Krenning EP, Bakker WH, Breeman WA, et al. Localisation of endocrine-related tumours with radioiodinated analogue of somatostatin. *Lancet*. 1989;1:242-244.
21. Krenning EP, Bakker WH, Kooij PP, et al. Somatostatin receptor scintigraphy with indium-111-DTPA-D-Phe-1-octreotide in man: metabolism, dosimetry and comparison with iodine-123-Tyr-3-octreotide. *J Nucl Med*. 1992;33:652-658.
22. Sundin A, Arnold R, Baudin E, et al. ENETS Consensus Guidelines for the Standards of Care in Neuroendocrine Tumors: Radiological, Nuclear Medicine & Hybrid Imaging. *Neuroendocrinology*. 2017;105:212-244.
23. Gabriel M, Decristoforo C, Kendler D, et al. ⁶⁸Ga-DOTA-Tyr3-Octreotide PET in Neuroendocrine Tumors: Comparison with Somatostatin Receptor Scintigraphy and CT. *Journal of Nuclear Medicine*. 2007;48:508-518.
24. Buchmann I, Henze M, Engelbrecht S, et al. Comparison of ⁶⁸Ga-DOTATOC PET and ¹¹¹In-DTPAOC (Octreoscan) SPECT in patients with neuroendocrine tumours. *European Journal of Nuclear Medicine and Molecular Imaging*. 2007;34:1617-1626.
25. Ambrosini V, Campana D, Bodei L, et al. ⁶⁸Ga-DOTANOC PET/CT Clinical Impact in Patients with Neuroendocrine Tumors. *Journal of Nuclear Medicine*. 2010;51:669-673.
26. Kwekkeboom DJ, Kam BL, van Essen M, et al. Somatostatin-receptor-based imaging and therapy of gastroenteropancreatic neuroendocrine tumors. *Endocr Relat Cancer*. 2010;17:R53-73.
27. Öberg K. Gallium-68 somatostatin receptor PET/CT: Is it time to replace ¹¹¹Indium DTPA octreotide for patients with neuroendocrine tumors? *Endocrine*. 2012;42:3-4.
28. Van Binnebeek S, Vanbilloen B, Baete K, et al. Comparison of diagnostic accuracy of ¹¹¹In-pentetretotide SPECT and ⁶⁸Ga-DOTATOC PET/CT: A lesion-by-lesion analysis in patients with metastatic neuroendocrine tumours. *European Radiology*. 2016;26:900-909.
29. Velikyan I, Sundin A, Sörensen J, et al. Quantitative and qualitative inpatient comparison of ⁶⁸Ga-DOTATOC and ⁶⁸Ga-DOTATATE: net uptake rate for accurate quantification. *J Nucl Med*. 2014;55:204-210.
30. Poeppel TD, Binse I, Petersenn S, et al. ⁶⁸Ga-DOTATOC Versus ⁶⁸Ga-DOTATATE PET/CT in Functional Imaging of Neuroendocrine Tumors. *Journal of Nuclear Medicine*. 2011;52:1864-1870.
31. Kabasakal L, Demirci E, Ocak M, et al. Comparison of ⁶⁸Ga-DOTATATE and ⁶⁸Ga-DOTANOC PET/CT imaging in the same patient group with neuroendocrine tumours. *Eur J Nucl Med Mol Imaging*. 2012;39:1271-1277.
32. Barrio M, Czernin J, Fanti S, et al. The Impact of Somatostatin Receptor-Directed PET/CT on the Management of Patients with Neuroendocrine Tumor: A Systematic Review and Meta-Analysis. *J Nucl Med*. 2017;58:756-761.
33. Sgouros G, Bolch WE, Chiti A, et al. ICRU REPORT 96, dosimetry-guided radiopharmaceutical therapy. *Journal of the ICRU*. 2021;21:1-212.
34. Cherry SR, Sorenson JA, Phelps ME. *Physics in Nuclear Medicine (Fourth Edition)*. Philadelphia: W.B. Saunders; 2012.

35. Tewson TJ, Welch MJ, Raichle ME. [18F]-labeled 3-deoxy-3-fluoro-D-glucose: synthesis and preliminary biodistribution data. *J Nucl Med.* 1978;19:1339-1345.
36. Strauss LG, Conti PS. The applications of PET in clinical oncology. *J Nucl Med.* 1991;32:623-648; discussion 649-650.
37. Kinahan PE, Fletcher JW. Positron Emission Tomography-Computed Tomography Standardized Uptake Values in Clinical Practice and Assessing Response to Therapy. *Seminars in Ultrasound, CT and MRI.* 2010;31:496-505.
38. Rahmim A, Lodge MA, Karakatsanis NA, et al. Dynamic whole-body PET imaging: principles, potentials and applications. *Eur J Nucl Med Mol Imaging.* 2019;46:501-518.
39. Lubberink M, Heurling K. Kinetic Modeling of Radiotracers. In: Lewis JS, Windhorst AD, Zeglis BM, eds. *Radiopharmaceutical Chemistry.* Cham: Springer International Publishing; 2019:501-514.
40. Gunn RN, Gunn SR, Cunningham VJ. Positron emission tomography compartmental models. *J Cereb Blood Flow Metab.* 2001;21:635-652.
41. van der Weerd AP, Klein LJ, Boellaard R, Visser CA, Visser FC, Lam-mertsma AA. Image-derived input functions for determination of MRGlu in cardiac (18)F-FDG PET scans. *J Nucl Med.* 2001;42:1622-1629.
42. Velikyan I, Sundin A, Sörensen J, et al. Quantitative and Qualitative In-trapatient Comparison of 68Ga-DOTATOC and 68Ga-DOTATATE: Net Up-take Rate for Accurate Quantification. *Journal of Nuclear Medicine.* 2014;55:204-210.
43. Patlak CS, Blasberg RG, Fenstermacher JD. Graphical evaluation of blood-to-brain transfer constants from multiple-time uptake data. *J Cereb Blood Flow Metab.* 1983;3:1-7.
44. Soret M, Bacharach SL, Buvat I. Partial-Volume Effect in PET Tumor Imag-ing. *Journal of Nuclear Medicine.* 2007;48:932-945.
45. Srinivas SM, Dhurairaj T, Basu S, Bural G, Surti S, Alavi A. A recovery coef-ficient method for partial volume correction of PET images. *Ann Nucl Med.* 2009;23:341-348.
46. Akerström G, Hellman P. Surgical aspects of neuroendocrine tumours. *Eur J Cancer.* 2009;45 Suppl 1:237-250.
47. Rinke A, Muller HH, Schade-Brittinger C, et al. Placebo-controlled, double-blind, prospective, randomized study on the effect of octreotide LAR in the control of tumor growth in patients with metastatic neuroendocrine midgut tu-mors: a report from the PROMID Study Group. *J Clin Oncol.* 2009;27:4656-4663.
48. Rinke A, Wittenberg M, Schade-Brittinger C, et al. Placebo-Controlled, Double-Blind, Prospective, Randomized Study on the Effect of Octreotide LAR in the Control of Tumor Growth in Patients with Metastatic Neuroendocrine Mid-gut Tumors (PROMID): Results of Long-Term Survival. *Neuroendocrinology.* 2017;104:26-32.
49. Kam BL, Teunissen JJ, Krenning EP, et al. Lutetium-labelled peptides for ther-apy of neuroendocrine tumours. *Eur J Nucl Med Mol Imaging.* 2012;39 Suppl 1:S103-112.
50. Kwekkeboom DJ, Teunissen JJ, Bakker WH, et al. Radiolabeled somatostatin analog [177Lu-DOTA0,Tyr3]octreotate in patients with endocrine gastroen-teropancreatic tumors. *J Clin Oncol.* 2005;23:2754-2762.
51. Kwekkeboom DJ, de Herder WW, Kam BL, et al. Treatment with the radio-labeled somatostatin analog [177 Lu-DOTA 0,Tyr3]octreotate: toxicity, effi-cacy, and survival. *J Clin Oncol.* 2008;26:2124-2130.

52. Bergsma H, van Vliet EI, Teunissen JJ, et al. Peptide receptor radionuclide therapy (PRRT) for GEP-NETs. *Best Pract Res Clin Gastroenterol.* 2012;26:867-881.
53. Kwekkeboom DJ, Bakker WH, Kam BL, et al. Treatment of patients with gastro-entero-pancreatic (GEP) tumours with the novel radiolabelled somatostatin analogue [177Lu-DOTA(0),Tyr3]octreotate. *Eur J Nucl Med Mol Imaging.* 2003;30:417-422.
54. Forrer F, Uusijarvi H, Storch D, Maecke HR, Mueller-Brand J. Treatment with 177Lu-DOTATOC of patients with relapse of neuroendocrine tumors after treatment with 90Y-DOTATOC. *J Nucl Med.* 2005;46:1310-1316.
55. Kwekkeboom DJ, Mueller-Brand J, Paganelli G, et al. Overview of results of peptide receptor radionuclide therapy with 3 radiolabeled somatostatin analogs. *J Nucl Med.* 2005;46 Suppl 1:62S-66S.
56. Bodei L, Cremonesi M, Grana CM, et al. Peptide receptor radionuclide therapy with (1)(7)(7)Lu-DOTATATE: the IEO phase I-II study. *Eur J Nucl Med Mol Imaging.* 2011;38:2125-2135.
57. Gabriel M, Andergassen U, Putzer D, et al. Individualized peptide-related-radionuclide-therapy concept using different radiolabelled somatostatin analogs in advanced cancer patients. *Q J Nucl Med Mol Imaging.* 2010;54:92-99.
58. Garske U, Sandstrom M, Johansson S, et al. Lessons on Tumour Response: Imaging during Therapy with (177)Lu-DOTA-octreotate. A Case Report on a Patient with a Large Volume of Poorly Differentiated Neuroendocrine Carcinoma. *Theranostics.* 2012;2:459-471.
59. Bodei L, Mueller-Brand J, Baum RP, et al. The joint IAEA, EANM, and SNMMI practical guidance on peptide receptor radionuclide therapy (PRRT) in neuroendocrine tumours. *Eur J Nucl Med Mol Imaging.* 2013;40:800-816.
60. Sgouros G, Bolch WE, Chiti A, et al. ICRU REPORT 96, Dosimetry-Guided Radiopharmaceutical Therapy. *Journal of the ICRU.* 2021;21:1-212.
61. Strosberg J, El-Haddad G, Wolin E, et al. Phase 3 Trial of (177)Lu-Dotatate for Midgut Neuroendocrine Tumors. *N Engl J Med.* 2017;376:125-135.
62. Strosberg J, Wolin E, Chasen B, et al. Health-Related Quality of Life in Patients With Progressive Midgut Neuroendocrine Tumors Treated With 177Lu-Dotatate in the Phase III NETTER-1 Trial. *Journal of Clinical Oncology.* 2018;36:2578-2584.
63. Brabander T, van der Zwan WA, Teunissen JJM, et al. Long-Term Efficacy, Survival, and Safety of [(177)Lu-DOTA(0),Tyr(3)]octreotate in Patients with Gastroenteropancreatic and Bronchial Neuroendocrine Tumors. *Clin Cancer Res.* 2017;23:4617-4624.
64. Emami B, Lyman J, Brown A, et al. Tolerance of normal tissue to therapeutic irradiation. *Int J Radiat Oncol Biol Phys.* 1991;21:109-122.
65. Benua RS, Cicale NR, Sonenberg M, Rawson RW. The relation of radioiodine dosimetry to results and complications in the treatment of metastatic thyroid cancer. *Am J Roentgenol Radium Ther Nucl Med.* 1962;87:171-182.
66. Bodei L, Cremonesi M, Ferrari M, et al. Long-term evaluation of renal toxicity after peptide receptor radionuclide therapy with 90Y-DOTATOC and 177Lu-DOTATATE: the role of associated risk factors. *Eur J Nucl Med Mol Imaging.* 2008;35:1847-1856.
67. Sundlöv A, Gleisner KS, Tennvall J, et al. Phase II trial demonstrates the efficacy and safety of individualized, dosimetry-based (177)Lu-DOTATATE treatment of NET patients. *Eur J Nucl Med Mol Imaging.* 2022;49:3830-3840.

68. Sandström M, Garske-Román U, Granberg D, et al. Individualized dosimetry of kidney and bone marrow in patients undergoing ¹⁷⁷Lu-DOTA-octreotate treatment. *J Nucl Med*. 2013;54:33-41.
69. Barone R, Borson-Chazot F, Valkema R, et al. Patient-specific dosimetry in predicting renal toxicity with (90)Y-DOTATOC: relevance of kidney volume and dose rate in finding a dose-effect relationship. *J Nucl Med*. 2005;46 Suppl 1:99S-106S.
70. Sandstrom M, Garske U, Granberg D, Sundin A, Lundqvist H. Individualized dosimetry in patients undergoing therapy with (177)Lu-DOTA-D-Phe (1)-Tyr (3)-octreotate. *Eur J Nucl Med Mol Imaging*. 2010;37:212-225.
71. Sjögreen Gleisner K, Chouin N, Gabina PM, et al. EANM dosimetry committee recommendations for dosimetry of ¹⁷⁷Lu-labelled somatostatin-receptor- and PSMA-targeting ligands. *Eur J Nucl Med Mol Imaging*. 2022;49:1778-1809.
72. Bolch WE, Eckerman KF, Sgouros G, Thomas SR. MIRD Pamphlet No. 21: A Generalized Schema for Radiopharmaceutical Dosimetry—Standardization of Nomenclature. *Journal of Nuclear Medicine*. 2009;50:477-484.
73. Stabin MG, Sparks RB, Crowe E. OLINDA/EXM: The Second-Generation Personal Computer Software for Internal Dose Assessment in Nuclear Medicine. *Journal of Nuclear Medicine*. 2005;46:1023-1027.
74. Del Prete M, Buteau FA, Beauregard JM. Personalized (177)Lu-octreotate peptide receptor radionuclide therapy of neuroendocrine tumours: a simulation study. *Eur J Nucl Med Mol Imaging*. 2017;44:1490-1500.
75. Garske-Román U, Sandström M, Fröss Baron K, et al. Prospective observational study of (177)Lu-DOTA-octreotate therapy in 200 patients with advanced metastasized neuroendocrine tumours (NETs): feasibility and impact of a dosimetry-guided study protocol on outcome and toxicity. *Eur J Nucl Med Mol Imaging*. 2018;45:970-988.
76. Council Directive 2013/59/Euratom. Official journal of the European Union. 2014;57.
77. van Essen M, Sundin A, Krenning EP, Kwekkeboom DJ. Neuroendocrine tumours: the role of imaging for diagnosis and therapy. *Nat Rev Endocrinol*. 2014;10:102-114.
78. Siebinga H, de Wit-van der Veen BJ, Beijnen JH, et al. A physiologically based pharmacokinetic (PBPK) model to describe organ distribution of (68)Ga-DOTATATE in patients without neuroendocrine tumors. *EJNMMI Res*. 2021;11:73.
79. Belhocine T, Foidart J, Rigo P, et al. Fluorodeoxyglucose positron emission tomography and somatostatin receptor scintigraphy for diagnosing and staging carcinoid tumours: correlations with the pathological indexes p53 and Ki-67. *Nucl Med Commun*. 2002;23:727-734.
80. Gabriel M, Oberauer A, Dobrozemsky G, et al. ⁶⁸Ga-DOTA-Tyr³-octreotide PET for assessing response to somatostatin-receptor-mediated radionuclide therapy. *J Nucl Med*. 2009;50:1427-1434.
81. Haug AR, Auernhammer CJ, Wängler B, et al. ⁶⁸Ga-DOTATATE PET/CT for the early prediction of response to somatostatin receptor-mediated radionuclide therapy in patients with well-differentiated neuroendocrine tumors. *J Nucl Med*. 2010;51:1349-1356.
82. Kratochwil C, Stefanova M, Mavriopoulou E, et al. SUV of [⁶⁸Ga]DOTATOC-PET/CT Predicts Response Probability of PRRT in Neuroendocrine Tumors. *Mol Imaging Biol*. 2015;17:313-318.

83. Oksuz MO, Winter L, PfannenberG C, et al. Peptide receptor radionuclide therapy of neuroendocrine tumors with (90)Y-DOTATOC: is treatment response predictable by pre-therapeutic uptake of (68)Ga-DOTATOC? *Diagn Interv Imaging*. 2014;95:289-300.
84. Velikyan I, Sundin A, Eriksson B, et al. In vivo binding of [68Ga]-DOTATOC to somatostatin receptors in neuroendocrine tumours--impact of peptide mass. *Nucl Med Biol*. 2010;37:265-275.
85. Kim SJ, Pak K, Koo PJ, Kwak JJ, Chang S. The efficacy of (177)Lu-labelled peptide receptor radionuclide therapy in patients with neuroendocrine tumours: a meta-analysis. *Eur J Nucl Med Mol Imaging*. 2015;42:1964-1970.
86. Strigari L, Konijnenberg M, Chiesa C, et al. The evidence base for the use of internal dosimetry in the clinical practice of molecular radiotherapy. *Eur J Nucl Med Mol Imaging*. 2014;41:1976-1988.
87. Glatting G, Bardiès M, Lassmann M. Treatment planning in molecular radiotherapy. *Z Med Phys*. 2013;23:262-269.
88. Chalkia MT, Stefanoyiannis AP, Chatziioannou SN, Round WH, Efstathopoulos EP, Nikiforidis GC. Patient-specific dosimetry in peptide receptor radionuclide therapy: a clinical review. *Australas Phys Eng Sci Med*. 2015;38:7-22.
89. Davis L, Smith AL, Aldridge MD, et al. Personalisation of Molecular Radiotherapy through Optimisation of Theragnostics. *J Pers Med*. 2020;10.
90. Huizing DMV, de Wit-van der Veen BJ, Verheij M, Stokkel MPM. Dosimetry methods and clinical applications in peptide receptor radionuclide therapy for neuroendocrine tumours: a literature review. *EJNMMI Res*. 2018;8:89.

Acta Universitatis Upsaliensis

*Digital Comprehensive Summaries of Uppsala Dissertations
from the Faculty of Medicine 1876*

Editor: The Dean of the Faculty of Medicine

A doctoral dissertation from the Faculty of Medicine, Uppsala University, is usually a summary of a number of papers. A few copies of the complete dissertation are kept at major Swedish research libraries, while the summary alone is distributed internationally through the series Digital Comprehensive Summaries of Uppsala Dissertations from the Faculty of Medicine. (Prior to January, 2005, the series was published under the title “Comprehensive Summaries of Uppsala Dissertations from the Faculty of Medicine”.)

Distribution: publications.uu.se
urn:nbn:se:uu:diva-486536



ACTA
UNIVERSITATIS
UPSALIENSIS
UPPSALA
2022